arXiv:1110.4043v1 [astro-ph.SR] 18 Oct 2011

# How well do we know the composition of the neutron star crust?

W. G. Newton, M. Gearheart, and Bao-An Li

*Department of Physics and Astronomy,*

*Texas A&M University-Commerce, Commerce, Texas 75429-3011, USA*

(Dated: October 19, 2011)

## Abstract

Within the liquid drop model, and using a phenomenological Skyrme-like parameterization of the uniform nuclear matter equation of state (EoS), we first construct a set of 'baseline' crustal equations of state that span the experimentally constrained values of the symmetry energy at nuclear saturation density, as well as the theoretically constrained region of the pure neutron matter (PNM) EoS at low density. The resulting range of crustal compositional parameters relevant for macroscopic models of the crust is explored, as well as the crust-core transition densities and pressures and the density range of the 'pasta' phases of nuclei at the bottom of the crust. We explore the deviation of these parameters from the baseline models as a result of the remaining experimental uncertainties in the symmetric nuclear matter (SNM) EoS and the parameterization of the surface energy in the liquid drop model. The transition densities and pressures are found to be quite sensitive to the behavior of the surface tension *at very low proton fractions*; recent calculations of the energies of neutron drops suggest that this might be higher than previously thought, which our study suggests may result in a much reduced volume of pasta in the crust. Most crustal compositional parameters are shown to be insensitive to the SNM EoS and the surface energy relative to the uncertainties in the symmetry energy, with the notable exception of the size of the nuclei which show a similar dependence on all the model parameters. We establish a set of crustal equations of state which can be matched with any core EoS based upon the symmetry energy and its derivative, allowing a consistent exploration of the dependence on the symmetry energy of global crustal models and potentially observable phenomena such as pulsar glitches and oscillation modes that incorporate a coupling between crust and core.

PACS numbers: 21.65.Cd,21.65.Ef,21.65.Mn,26.60.Gj,26.60.Kp,97.60.Jd

## I. INTRODUCTION

The increasing wealth and sensitivity of observations associated with neutron star systems is demanding ever more sophisticated theoretical models of their structure and dynamics from micro- to macro-scopic scales. Many proposed theoretical models for observed phenomena, such as pulsar glitches, or potentially observable phenomena, such as gravitational waves from stellar oscillations or deformations of the star, involve incorporating global properties of the star, properties of the elastic crust, and the coupling between the two [1–6].

One goal of neutron star physics is to make use of the available observations to provide data complimentary to those provided by terrestrial nuclear experiments in order to better understand the microphysics of dense matter [7]. In order to extract microphysical constraints from observations, the theoretical description of the observations should ideally use consistent models of the nuclear physics throughout the star in describing the properties of the matter. Simple global properties of a neutron star such as its mass, radius and total moment of inertia are relatively insensitive to the properties of the crust itself, which contributes a small fraction of the total to each; in such cases the dominant theoretical ingredient is the nuclear equation of state (EoS) for the core [8]. However, in models where the crust-core interplay is important there will be a sensitivity to both global and microscopic core and crust properties. That the dominant uncertainties in the nuclear EoS can be usefully encoded in the nuclear symmetry energy is well known. The dependence of global stellar properties such as the radius, and crustal properties such as its thickness on the symmetry energy has also been well studied. However, little attention has been paid to the relationship between the symmetry energy, crust properties, and global properties in a consistent way. This paper aims to provide one step towards such a consistent approach.

The outer and inner layers of the neutron star crust are defined by the absence and presence of a neutron fluid external to the nuclear clusters respectively. Additionally, a third layer is often predicted to be present at the bottom of the inner crust, consisting of exotic nuclear geometries collectively termed nuclear 'pasta'; this layer may be called the mantle [9]. The mantle can contain two distinct sub-layers: (1) the layer in which the pasta structures contain nuclear matter of non-zero proton fraction, surrounded by a fluid of pure neutron matter ('normal pasta'); (2) the inverse situation in which the pasta structures are bubbles containing pure neutron matter, surrounded by a higher density fluid of nuclear matter with a non-zero proton fraction ('bubble pasta'). In the latter layer, protons themselves are macroscopically free. Whether these layers are to be included when modeling the bottom of the inner crust and the transition to the neutron star core will have important consequences for the physics of the crust-core interface.

Global properties of neutron stars such as mass and radius are relatively insensitive to the crust EoS $P(\rho)$. However, there are a number of important crustal quantities that are sensitive to the crustal composition and thickness, both of which depend on the uniform nuclear matter EoS, the energy density of a homogeneous fluid of neutrons and protons as a function of density and proton fraction. In particular, as crustal matter comprises relatively low- or zero -proton fraction nuclear matter, crustal properties are sensitive to the symmetry energy of the nuclear EoS, which describes how the energy density changes as proton fraction varies [10, 11]. Experimental effort has focussed on constraining the magnitude of the symmetry energy at saturation density $J$, and the derivative of the symmetry energy with respect to density $L$.

The density at which the transition from the crust to the core occurs has been shown to be sensitive to $L$ [10, 12**?** ], and hence the volume fraction occupied by the crust. The mass and moment of inertia fraction of the crust, important in the modeling of pulsar glitches [1], is sensitive to the transition pressure, which has been shown to correlate with the slope and curvature of the symmetry energy around saturation density [14]. The maximum and typical size of mountains on NS crusts [15, 16] and frequencies of torsional crustal oscillations [17–20] depends on the thickness of the elastically rigid part of the crust and its shear modulus, which depends on the characteristic quantities which define the lattice: the inter-ion spacing $a$ and nuclear charge $Z$ [2]. The shear modulus throughout the inner crust [21–23] is an important quantity in determining the frequencies at which the crust might undergo global oscillations. Various transport properties within the crust will also depend somewhat on the crustal composition through the densities of the various components, the electron fraction and the lattice spacing. The region of densities at which the neutrons are predicted to form a superfluid via the $^1\mathrm{S}_0$ channel has a model dependence; the possibility of layers of the crust in which the neutron fluid is normal exists, and will depend on the crust-core transition density, and the existence of a neutron superfluid in the pasta layers will also depend on their extent. Also, the melting temperature of the crustal lattice depends on the compositional parameters, and its magnitude relative to the superfluid transition density will impact the dynamics of the crust.

The 'pasta' phases [24, 25] might have very different behaviors to the purely crystalline phase. The shear modulus of the pasta phases is still very uncertain, and will have a large effect on the crust-core boundary layer, of particular importance to the damping of r-mode oscillations [4] and the spectrum of torsional oscillations [2]. The phases of bubble nuclei may allow the direct URCA neutrino cooling process [9]. Thermodynamic and neutrino scattering properties of the pasta phases could be rather different [26–28]. The extent of the pasta phases in the crust will determine the importance of those phases to crustal processes and the dynamics of the crust-core coupling. The region of the inner crust occupied by the 'pasta' phases is also strongly dependent on $L$, since, while the density of transition to pasta remains roughly constant in a given model [10], the crust-core transition density decreases with increasing $L$, reducing the density range of the pasta phases at higher $L$.

The compressible liquid drop model (CLDM) [29] has proven to be a useful tool for the study of neutron star crust [11, 24, 26–28, 30–39]. Like the liquid drop and droplet models of terrestrial nuclei, the CLDM focusses on the average, macroscopic properties of nuclear clusters in the crust such as mass and radius, whilst neglecting the quantum shell effects. The interior nuclear density is a free variable (hence compressible) rather than specified *a priori* as the saturation density of symmetric nuclear matter (SNM). An external gas of dripped neutrons, expected to coexist with the nuclear clusters in the inner crust, is calculated using the same bulk Hamiltonian as the matter inside the clusters. The neutron star inner crust is assumed to have the structure of a regular lattice, and the Wigner-Seitz (WS) approximation is employed in which the unit cell, which generally will have a cubic or more complicated structure, can be replaced by a spherical cell of the same volume. The W-S approximation is good so long as the nuclear size is much smaller than the cell size, but breaks down when the two sizes become comparable. Despite the two approximations, the CLDM provides a good description of the average microscopic properties of the neutron star crust, including the energetically preferred nuclear mass, size, WS cell size and density of dripped neutrons. Its amenability to quick calculation, and physical transparency, have made it the most widely used model for the computation of the EoS and composition of the inner neutron star crust and of inhomogeneous nuclear phases in core collapse supernovae [29, 40, 41]; it is therefore important to understand its limitations and accuracy given the experimental and theoretical uncertainty in its model parameters.

The purpose of this paper is to (i) provide a 'baseline' set of inner crust EoSs generated by varying the slope of the symmetry energy within limits imposed by terrestrial experiments and theoretical pure neutron matter (PNM) calculations, together with their associated crust compositions, such that a suitable crust EoS can be found to match a core EoS with the same symmetry energy behavior, and (ii) systematically explore the remaining model dependence of the crustal composition, focussing on the experimental and theoretical uncertainties of the SNM EoS and the surface energy. In section II we outline the CLDM. In section III we describe our model for the bulk nuclear matter EoS, and the experimental and theoretical PNM constraints we will use. In section IV we discuss the range of parameters used in the proscription for the surface energy. In section V we present the set of baseline results, before probing the surface energy and SNM EoS dependence of the crust composition in sections VI and VII, and the dependence of the PNM EoS at intermediate densities in section VIII. In section IX we discuss how the EoS and surface uncertainties can impact important crustal properties such as its shear modulus and melting temperature, and we conclude in section X.

## II. THE COMPRESSIBLE LIQUID DROP MODEL

We use the CLDM originally formulated by BBP [29] and updated to incorporate non-spherical nuclear shapes by Watanabe, Iida and Sato [26, 27, 39]. For completeness, we recall the main ingredients of the CLDM. Assuming a regular crystal structure for crustal matter, a repeating unit cell can be identified in which a single nucleus (or nuclear cluster) containing all the protons of the cell resides immersed in an external, uniform neutron fluid. A homogeneous gas of electrons is present to neutralize the positive protonic charge. We consider the five canonical nuclear geometries (the 'pasta' shapes): spherical, cylindrical, planar, cylindrical bubble and spherical bubble. The dimensionality of the shapes are specified by a parameter $d = 3, 2, 1$ for spherical, cylindrical and planar geometries respectively. The Wigner-Seitz (WS) approximation is employed, in which the actual unit cell is replaced by an equally volumed unit cell of spherical, cylindrical or planar geometry depending on the pasta shape chosen.

$$\varepsilon_{\rm cell}(r_{\rm c}, x, n, n_{\rm n}) = v\left[nE(n,x)+\varepsilon_{\rm exch}+\varepsilon_{\rm thick}\right]+u\varepsilon_{\rm surf}+u\varepsilon_{\rm Coul}+(1-v)n_{\rm n}E(n_{\rm n},0)+\varepsilon_{\rm e}(n_{\rm e}) \quad (1)$$

$E(n,x)$ is the energy per particle of uniform nuclear matter, $\varepsilon_{\text{Coul}}$ the Coulomb energy including the proton-proton and proton-electron interactions, $\varepsilon_{\text{surf}}$ is the surface energy and $\varepsilon_{\text{e}}(n_{\text{e}})$ is the electron energy. $u = (r_{\text{N}}/r_{\text{c}})^d$ is the volume fraction occupied by the nuclei or the bubble of radius $r_{\text{N}}$, dimension $d$, and

$$v = \begin{cases} u & \text{nuclei} \\ 1-u & \text{bubble} \end{cases} \tag{2}$$

is the volume fraction of matter of non-zero proton fraction, and distinguishes nuclei from bubble phases in equation (1). The independent variables are taken to be the WS cell radius $r_{\text{c}}$, the density and proton fraction inside the nuclear cluster $n, x$ and the neutron fluid density $n_{\text{n}}$. The electron number density $n_{\text{e}}$ is related to these variables via the charge neutrality condition $n_{\text{e}} = unx$.

The global baryon number density is related to these variables through the relation

$$n_{\text{b}} = vn + (1-v)n_{\text{n}} \tag{3}$$

from which we can define the fraction of nucleons in the neutron fluid $X_{\text{n}} = (1-v)n_{\text{n}}/n_{\text{b}}$ and in the nuclear cluster $X_{\text{nuc}} = vn/n_{\text{b}}$ such that $X_{\text{n}} + X_{\text{nuc}} = 1$.

The Coulomb energy, which includes the lattice energy (the proton-electron contribution) is given in the WS approximation by

$$\varepsilon_{(C+L)} = 2\pi(exnr_N)^2 f_d(u) \tag{4}$$

$$f_d(u) = \frac{1}{d+2}\left[\frac{1}{d-2}\left(1 - du^{1-2/d}\right) + u\right]. \tag{5}$$

The surface thickness correction from BBP [29] and the proton Coulomb exchange energy are given by

$$\varepsilon_{thick}(k,x) = -\frac{4}{9}\pi e^2 w^2 x^2 k^3 n \tag{6}$$

$$\varepsilon_{exch}(k,x) = -\frac{3}{4\pi}2^{1/3}e^2 x^{4/3} kn \tag{7}$$

where $k = (1.5\pi^2 n)^{1/3}$ and $w$ is a distance representing the surface thickness, taken to be $w \approx 0.75$ fm. The energy density of the free electron gas is taken to be simply the free Fermi gas expression

$$\varepsilon_{\text{e}} = \frac{9}{8}\hbar c\pi^{2/3}(xnu)^{4/3}, \tag{8}$$

neglecting electron screening.

The composition of the cell is obtained by minimizing the energy of the unit cell with respect to the free parameters. This produce four relations which correspond physically to mechanical, chemical and beta equilibrium of the cell plus the nuclear virial relation

$$\epsilon_{\rm coul} = 2\epsilon_{\rm surf} + \epsilon_{\rm curv} \tag{9}$$

which expresses equilibrium with respect to variation of relative volumes of the two phases in the unit cell.

To simplify our model, we neglect electron screening and the effect of a neutron skin to the nuclear clusters. Shell effects both in the nuclei and the dripped neutron fluid are not taken into account in this classical model, and the WS approximation is expected to break down at the highest densities in the crust [42]. In a later work, using a microscopic calculation, we will assess the effects of these approximations and missing physics using the results of this paper as a comparison.

## III. THE EQUATION OF STATE OF UNIFORM NUCLEAR MATTER

Useful parameters characterizing the EoS of isospin asymmetric nuclear matter around SNM (proton fraction $x = 0.5$; $\delta = 0$) and the saturation density of SNM $n_{\rm s}$ can be derived by expanding $E(n,x)$ in a power series in the isospin asymmetry $\delta = 1-2x$ and the density parameter $\chi = \frac{n-n_0}{3n_0}$

$$E(n,x) = E_0(n) + S(n)\delta^2 + ... \tag{10}$$

$$E_0(n) = E_0 + \tfrac{1}{2}K_0\chi^2 + ... \tag{11}$$

$$S(n) = J + L\chi + \tfrac{1}{2}K_{sym}\chi^2 + ... \tag{12}$$

$$E_{\rm PNM}(n) \approx E_0(n) + S(n) \tag{13}$$

$E_0(n) = E(n, 0.5)$ is the binding energy per nucleon of SNM and $S(n) = \frac{1}{2}\partial^2 E(n,x)/\partial\delta^2_{x=0.5}$ is the nuclear symmetry energy. $K_0$ is the incompressibility of SNM at saturation density. $J = S(n_0)$, $L = \partial S(n)/\partial\chi|_{n=n_0}$ and $K_{\rm sym}$ are the value of the symmetry energy, its slope and its curvature at saturation density. In particular, the pressure of pure neutron matter at sub-saturation densities, which plays a large role in determining the equilibrium composition of the crust, can be expressed as

$$P = \frac{n^2}{3n_0}[L + (K_0 + K_{\rm sym})\chi + ...]. \tag{14}$$

to the leading two orders.

Throughout most of this paper we will mainly use the modified Skyrme-like (MSL) parameterization of the nuclear matter EoS $E(n, \delta)$ [43] (see appendix A) as our description of uniform nuclear matter as a function of density and isospin asymmetry. Like the Skyrme parameterization, the MSL model has a number of free parameters; these parameters can be analytically related to the properties of uniform nuclear matter at saturation density, allowing a smooth variation of, e.g., the symmetry energy at saturation $J$ and its slope $L$. For comparison, we will also use a similar phenomenological EoS whose form was originally written down by Bludman and Dover [44] (which we will refer to as BD, see also appendix A), which was later modified and used to study finite nuclei and inner crust composition by Oyamatsu and Iida [10, 45], and a selection of Skyrme EoSs [46] whose basic properties are given in Table 1.

We note that for all of these EoSs, the symmetry energy is calculated in full without the use of the parabolic approximation (PA) in which one truncates the expansion in equation (10) at second order, thus obtaining the symmetry energy as $S(n) = E_{\mathrm{PNM}}(n) - E_0(n)$. Although, in many circumstances, the parabolic approximation is good enough, since the coefficients of fourth order and higher are small, it has been shown [13, 14] that for selected crustal properties, most notably the crust-core transition density, the PA can lead to divergent predictions compared to the full EoS.

TABLE I: Skyrme parameters. $J$, $L$, and $K_0$ are in MeV, $n_0$ in fm$^{-3}$.

| | $J$ | $L$ | $K_0$ | $n_0$ |
|---|---|---|---|---|
| SLy4 | 32.04 | 46.03 | 230.31 | 0.16 |
| SkM* | 30.06 | 45.79 | 216.97 | 0.161 |
| BSk14 | 30.03 | 43.94 | 239.74 | 0.159 |
| BSk16 | 30.02 | 34.89 | 242.08 | 0.159 |
| NRAPR | 32.82 | 59.69 | 226.06 | 0.161 |
| SII | 34.15 | 50.07 | 341.19 | 0.148 |
| SkI4 | 29.54 | 60.51 | 248.41 | 0.16 |
| SkX | 31.11 | 33.14 | 271.48 | 0.156 |

### A. Experimental constraints on the symmetry energy

The magnitude of the symmetry energy at saturation density $J$ is constrained mainly from nuclear mass model fits to experimental data [47–50]. Care must be taken when interpreting predictions for $J$, since often different definitions for the symmetry energy at saturation are used, for example differing in the use of the parabolic approximation. Moreover, in mass model fits, $J$ depends significantly on what surface symmetry energy is used, e.g. [51]. We take as a conservative range $25 < J < 35$ MeV.

Constraints on the density dependence of the nuclear symmetry energy have been obtained in analyses of a variety of nuclear experimental data [52, 53]. Recent modeling of isospin diffusion in heavy ion collisions involving $^{112}$Sn and $^{124}$Sn extracted constraints of $62< L <107$ MeV using the IBUU04 transport model [54, 55] and $45< L <103$ MeV using the ImQMD molecular dynamics model [53] respectively. The extraction of the range of $L$ is model dependent; the two ranges quoted here, whereas they overlap significantly, are from the two different transport model analyses. A study of isoscaling data from multifragmentation reactions yields $L \sim 66$ MeV [56]. A constraint from the analysis of pygmy dipole resonance (PDR) data gives $27< L <60$ MeV [57] and from the analysis of the surface symmetry energies of nuclei over a wide range of masses gives $75< L <115$ MeV [58]. A measurement of neutron skins of a wide mass range of nuclei has led to an estimate of $25< L <100$ MeV [59]. Combining data on the neutron skin thickness of Sn isotopes and isospsin diffusion and double n/p ratios in heavy ion collisions, a range of $40 < L < 70$ MeV is obtained [60], while constraints on the global nucleon optical potential from nucleon-nucleus reactions and single particle energy levels of bound nuclear states leads to a range $30.2 < L < 75.2$ MeV [61]. For the latest and more extended discusssions on the experimental constraints on $J$ and $L$, we refer the reader to the NuSYM11 (Nuclear Symmetry Energy Workshop 2011) website [62]. We take as a conservative range $25 < L < 115$ MeV, noting however that more recent studies favor the lower half of this range [50, 63].

As a representation of the above uncertainties, we focus on the PNM EoS as this enables us to make contact with microscopic calculations the predictions of which, at low densities, are now quite robust. For a given model, the SNM EoS ($\delta = 0$) and the symmetry energy fixes the PNM EoS. The PNM EoS for the MSL and BD models at a constant value of $J = 35$ MeV with $L = 25, 70, 115$ MeV are plotted in the left panels of Fig. 1. For constant

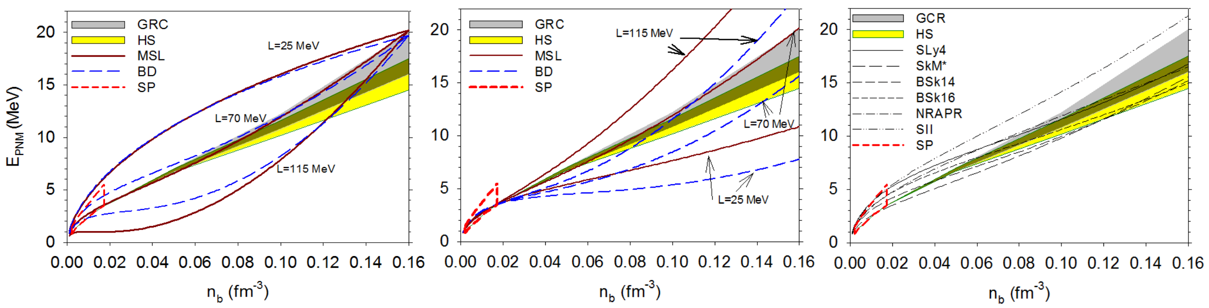

FIG. 1: (Color online) PNM energy per particle versus baryon number density for the MSL and BD EoSs with $J$=35 MeV (left), constraining the MSL and BD EoSs to fit the low-density end of the PNM EoS from microscopic calculations (middle) and for a selection of Skyrme EoSs (right). The gray and dotted bands correspond to the microscopic calculations of Gandolfi et al [69] (GCR) and Hebeler and Schwenk [68] (HS) taking into account uncertainties in the three-nucleon interaction, while the boxed region at low density comes from the calculations of Schwenk and Pethick [66] (SP).

$J$, the MSL and BD EoSs match closely for low densities and high values of $L$.

## B. Theoretical constraints on the pure neutron matter EoS

Theoretically, the PNM EoS has recently been well constrained at low densities through quantum Monte-Carlo, Green's function Monte-Carlo, chiral effective field theory and variational chain summation techniques [64–68]. These constraints, which are expected to be quite robust, may be taken as a constraint for our uniform nuclear matter EoS. We show the PNM constraint from Schwenk and Pethick (SP) [66] as the red box at low densities; results since have converged on the lower bound of that box. Calculations at higher sub-saturation densities introduce uncertainties which are dominated by the theoretical uncertainties in the three-nucleon force; two recent calculations with estimated theoretical error bars have been performed [68, 69] (labelled HS, GCR hereafter, respectively), and are indicated by the shaded bands in Fig. 1.

In the left panel of Fig. 1, one can see that our phenomenological EoSs at a constant value of $J$ are consistent only for a very limited range of $L$ (e.g. $L \approx 70$ MeV for $J = 35$ MeV for the MSL EoS). We thus explore the effect of constraining our phenomenological

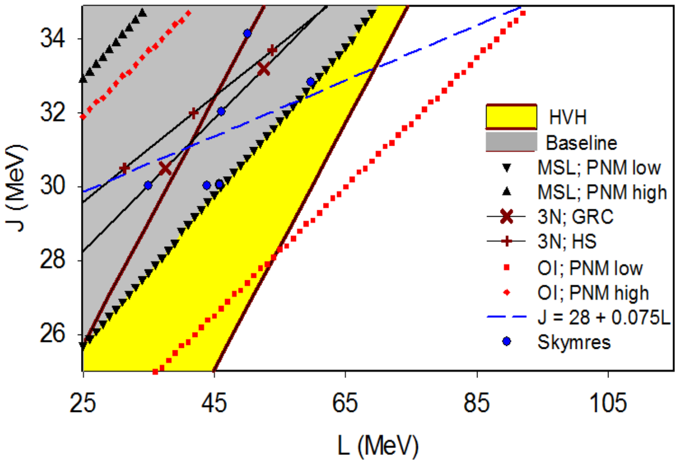

FIG. 2: (Color online) Correlation between $J$ and $L$ obtained by requiring the MSL EoS pass through the upper bound from low density PNM calculations (upwards pointing triangles) and the lower bound (downwards pointing triangles); the gray shaded region indicates the region consistent with the PNM constraints. The yellow band is obtained by applying the Hugneholtz-van-Hove theorem to optical potential data [70], the black lines from PNM calculations at higher densities (red plusses - chiral perturbation theory [68]; red crosses - QMC methods [69]) and the blue lines from constraints on the saturation properties of asymmetric matter from mass fits [10].

EoSs using PNM calculations as follows.

We constrain our MSL and BD EoSs given a reference low density PNM EoS for a given value of $L$ by varying the magnitude of the symmetry energy at saturation $J$ for that $L$ until our phenomenological PNM EoS passes through the reference EoS. For another value of $L$, $J$ must be readjusted so that we match the reference EoS again. In the middle panel of Fig. 1, we plot the MSL and BD PNM EoS following such procedure, with the reference EoS at *low* densities taken to be the results of HS and GCR which closely coincide with the lower bound of the SP box. We show results for $L = 25, 70$ and 115 MeV. For a given value of $L$, and applying the low density PNM constraint, the MSL and BD EoSs differ significantly, with the BD PNM energy being appreciably lower for most of the density range up to saturation (corresponding to a lower symmetry energy $J$); thus the BD EoS will give a lower pressure of PNM. Finally, we display a selection of Skyrme PNM EoSs in the right panel of Fig. 1; the selection was made based on the criterion that they pass through the SP constraint.

One trivial consequence of applying this constraint is that we are no longer free to vary $J$

independently of $L$; we select only those EoSs in J-L space which conform to the low density PNM constraints, thus imposing a correlation between the symmetry energy and its slope at saturation density. This correlation is shown in Fig. 2 for the MSL EoS by the upright black triangles (for the upper bound of the SP constraint) and the lower black triangles (for the lower bound), and for the BD EoS by the squares and diamonds respectivley. Taking the upper or lower bounds of the SP constraint produces a different offset to the correlation without changing its slope. The existence of such a correlation is in part due to the variation of the PNM EoS with density; all theoretically derived energy-density functions are simple enough to admit such a correlation. For example, a correlation derived from the low density PNM constraint might not exist if the energy of PNM is not a monotonic function of density in the region up to saturation density. This, however, would imply a region of density in which PNM became stable, a phenomenon that we would expect to have seen indications of in nuclear experiments. Given a smooth, monotonically increasing function of density, a constraint at the low density end will give a correlation between its value at the higher density region, and its slope there.

Although our correlation is simply a result of applying the PNM constraint, such a correlation has been noted in several other works, also plotted in Fig. 2. The PNM calculations can be extended towards saturation density and beyond with the inclusion of uncertain three-body forces; given an empirical value for the symmetry energy at saturation, one then obtains a value for $L$. Correlations in the $J-L$ plane are shown for two such recent studies [68, 69]. The Hugenholtz-Van-Hove theorem predicts a relation between $J$ and $L$ whose uncertainty, in the symmetry potential, can be related to nucleon optical potentials; in the analysis of Xu et al [70], the yellow shaded region in Fig. 2 is predicted. Oyamatsu and Iida [10], hereafter OI, obtained a constraint from fits to nuclear masses and charge radii using the BD EoS of $S = 28 + 0.075\ L$. Finally, our selection of Skyrmes are also plotted. As can be seen, there is some variation in the slope of the correlation and its offset from the $L$ axis, but the studies so far predict correlations that favor the low-$L$, high $J$ half of the plane, in which our correlation also falls. The OI results show that two different correlations can be obtained for the same EoS depending on the data used to obtain it.

## IV. THE SURFACE ENERGY

The surface energy density can be written in terms of the surface tension $\sigma_{\rm s}$ as

$$\varepsilon_{surf} = \frac{d\sigma_{\rm s}}{r_N}, \tag{15}$$

where $r_{\rm N}$ is the radius of the nuclear cluster (half-width in the case of planar clusters) and $d$ the dimensionality of the cluster. In order to take into account the effect of the curvature of the nuclear surface, a curvature correction is added:

$$\sigma_{\rm s} \to \sigma_{\rm s} + (d-1)\sigma_{\rm c}/r_{\rm N}, \tag{16}$$

where $\sigma_{\rm c}$ is the curvature tension.

Analogously to nuclear matter, the surface and curvature tension may also be expanded about its isospin symmetric value:

$$\sigma_{\rm s}(x) = \sigma_0 + \sigma_\delta \delta^2, \tag{17}$$

$$\sigma_{\rm c}(x) = \sigma_{{\rm c},0} + \sigma_{{\rm c},\delta}\delta^2, \tag{18}$$

where $\sigma_\delta = \frac{1}{2}\partial^2\sigma_{\rm s}/\partial\delta^2|_{x=0.5}$ is the symmetry surface tension; the symmetry curvature tension is defined similarly.

The first formulations of the CLDM parameterized the surface energy in terms of the proton fraction $x$, the bulk nuclear and neutron matter densities $n, n_{\rm n}$, and the difference in energy per particle between the two bulk phases [29–31, 39] inspired by one- and two-fluid Thomas-Fermi theory. It was noted that, in fact, the surface energy is to be evaluated along the curve of coexistence between the bulk nuclear and pure neutron matter [71, 72] and therefore the quantities upon which it depends $n, x, n_{\rm n}$ are not all independent variables. At zero temperature, the surface tension may be parameterized in terms of one variable, which is most conveniently chosen to be the proton fraction $x$. The inclusion of a neutron skin accounts for the dependence of surface properties on the bulk nuclear densities. In this work we omit the neutron skin; the effects of the skin will be examined in a subsequent study. Here we use the parameterization first used by Lattimer, Pethick, Ravenhall and Lamb (LPRL) [71, 72], which was subsequently generalized by Lorenz and Pethick [73, 74]:

$$\sigma_{\rm s} = \sigma_0 \frac{2^{p+1} + b}{\frac{1}{x^p} + b + \frac{1}{(1-x)^p}}, \tag{19}$$

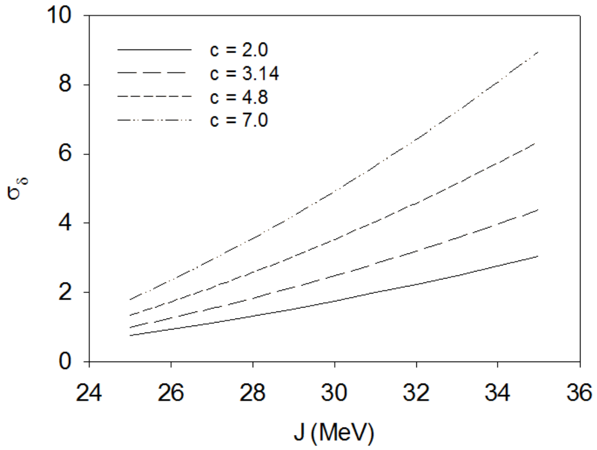

FIG. 3: Surface symmetry parameter $\sigma_{\rm sym}$versus symmetry energy $J$ for four values of the surface symmetry - volume symmetry correlation.

from which we can derive

$$\sigma_\delta = \sigma_0 \frac{2^p p(p+1)}{2^{p+1}+b}. \tag{20}$$

The curvature tension takes the form [73, 74]

$$\sigma_{\rm c} = \sigma_{\rm s}\frac{\sigma_{0,\rm c}}{\sigma_0}\alpha(\beta - x) + \gamma x^4. \tag{21}$$

The parameters $\sigma_0, \sigma_{0,\rm c}, b, p, \alpha, \beta, \gamma$ are adjusted to fit calculations of the interface between two different phases of semi-infinite nuclear matter using the Thomas-Fermi and Hartree-Fock methods [38, 73].

### A. Constraints on the surface energy

Experimentally, $\sigma_0$, $\sigma_{\rm c}$ and $\sigma_\delta$ are determined largely by fitting liquid drop models to nuclear mass data [11, 48, 51, 75–78]. The values obtained are rather dependent on the formulation of the liquid drop model. The strength of the surface and curvature tensions for SNM are relatively well determined to be in the range of $1.0 \lesssim \sigma_0 \lesssim 1.1$ MeV fm$^{-2}$, $0.5 \lesssim \sigma_{\rm c,0} \lesssim 0.6$ MeV fm$^{-1}$; in our model we fix $\sigma_0 = 1.1$ MeV fm$^{-2}$ and $\sigma_{\rm c,0} = 0.6$ MeV fm$^{-1}$. The surface symmetry energy is rather more model dependent; that uncertainty can be systematically encoded in the correlation which exists between the surface symmetry energy and the bulk symmetry energy $J$. The correlation emerges both from fits to nuclear

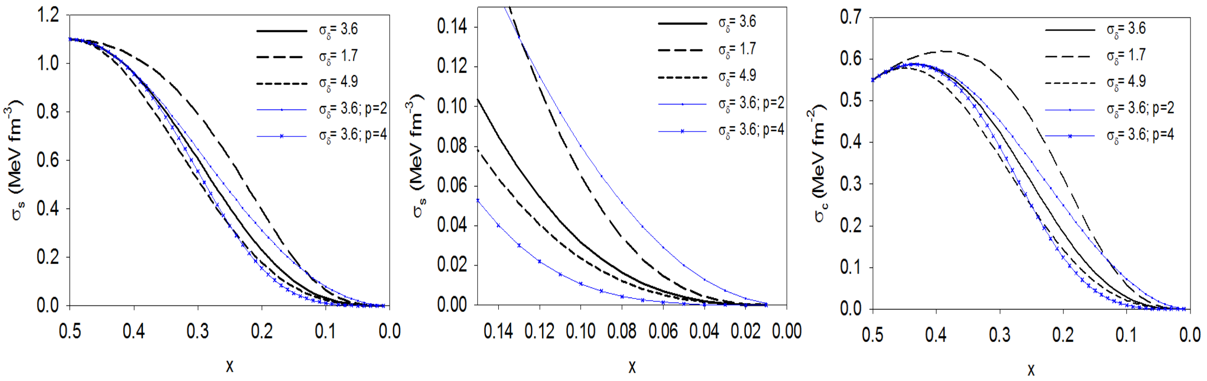

FIG. 4: (Color online) Form of the surface and curvature potentials used in this work for 3 different values of the surface symmetry energy and 2 different parameterizations of the low proton fraction behavior.

masses and from calculations of the properties of plane interfaces; the slope of the correlation depends on the model used [77, 78]. We incorporate this correlation as follows:

$$\sigma_\delta = \frac{E_{\rm sym} n_{\rm s}^{2/3}}{(36\pi)^{1/3}\sigma_0}[(0.046c + 0.01)E_{\rm sym} - c] \tag{22}$$

where $c$ gives the slope of the correlation. In Steiner et al [77] a comprehensive study was conducted of the extraction of the surface symmetry energy from mass model fits and microscopic calculations of plane interfaces between two different phases of nuclear matter. The surface symmetry energy was extracted using two different, thermodynamically consistent formulations of the surface thermodynamic potential in the mass model; the so-called '$\mu_{\rm n}$' and '$\mu_\alpha$' approaches which differ in the way the neutron skin is taken into account. The best fits obtained for the '$\mu_{\rm n}$' and '$\mu_\alpha$' approaches are given by $c = 3.14$ and $c = 4.8$ respectively in equation (22); the full region of the surface symmetry - bulk symmetry energy plane can be spanned by $c = 2.0$ to $c = 7.0$. In our model, we impose the correlation in equation (22) and take for our baseline results $c = 4.8$. We can then explore the effect of the correlation systematically by varying $c$ over the full range from $c = 2.0$ to $c = 7.0$. In Fig. 3 this range is depicted. In Fig. 4 we show the form for the surface and curvature potentials for 3 different values of the surface symmetry energy $\sigma_\delta$ corresponding to $J = 30$ MeV, $c = 2$, 4.8 and 7 by the black solid, long-dashed and short dashed lines respectively.

Of particular importance is the behavior of the surface energy at low proton fractions, determined in equation (19) by the parameter $p$. Although the fits to plane interface calculations suggest a value of $p = 3$, these were performed using Skyrme interactions. Recent work on neutron drops suggests that the gradient terms in the Skyrme interactions underestimate the surface energy for pure neutron matter [79]. We will therefore also vary $p$ in the range 2 - 4 to determine the relative importance of the low proton fraction surface energy. In Fig. 4 we also show the form of the surface and symmetry energy for $p$=2 and 4 for $\sigma_\delta$ = 3.6 corresponding to $c = 4.8, J = 30$ MeV. The middle panel shows a close-up of the low proton fraction region of the surface potential, emphasizing the fact that $p = 4$ gives a higher surface tension in this region, $p = 2$ a lower surface potential.

## V. BASELINE RESULTS

Our baseline SNM EoS and surface parameters are summarized in Table 2. We then vary the slope of the symmetry energy $L$ from 25 - 115 MeV under two different constraints:

- Constant symmetry energy at saturation density $J$. Varying $J$ over the range 25 - 35 MeV generates a new sequence of EoSs over the range of $L$; we will use as a shorthand label for such a sequence at, say $J = 35$ MeV, 'J35'
- Demanding a specific PNM EoS at low densities; then $J$ will vary with $L$ according to the correlations given in Fig. 2. We will concentrate on the lower bound of the SP constraint outlined in Figs. 1 and 2; we will label the sequence of crust EoSs generated by such a sequence as 'PNM'.

In our model, the region of the $J, L$ parameter space consistent with both the conservative experimental range of $J = 25 - 35$ MeV and the theoretical PNM constraint corresponds to the shaded gray region in Fig. 2; the corresponding region for the various crustal properties will also be shown as a shaded region in subsequent plots. We also note that, since the recent results from PNM calculations are expected to be quite robust, and give a low density PNM

TABLE II: Baseline parameters

| $K_0$ (MeV) | $n_0$(fm$^{-3}$) | $\sigma_0$ (MeV fm$^{-2}$) | $\sigma_{c,0}$(MeV fm$^{-1}$) | $c$ | $p$ |
|---|---|---|---|---|---|
| 240 | 0.16 | 1.1 | 0.6 | 4.8 | 3 |

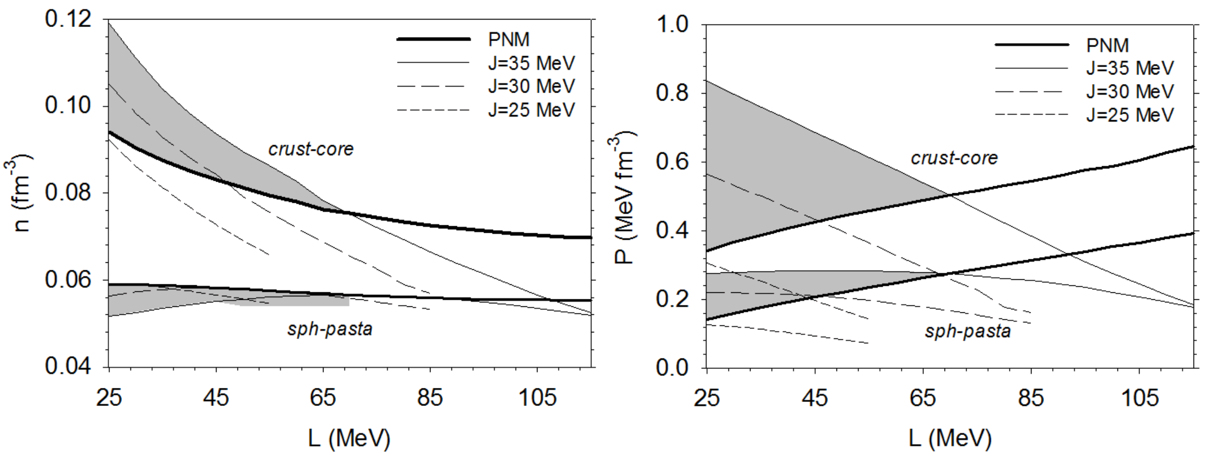

FIG. 5: Crust-core and spherical nuclei-pasta transition densities (left) and pressures (right) versus $L$. Results are displayed for the 3 constant-J sequences ‘J35’, ‘J30’ and J25’ and the two sequences constrained by the low density PNM EoS ‘PNM’. The shaded region correspond to the region consistent with the PNM constraint and $25 < J < 35$ MeV.

EoS at the lower bound of the SP constraint, the ‘PNM’ sequence gives the most stringent constraint on crust properties within our model.

We will concentrate on the crust-core, and ‘normal’ (spherical) nuclei - pasta (cylindrical phase) transition densities and pressures ($n_{\rm cc}, n_{\rm p}, P_{\rm cc}, P_{\rm p}$ respectively), and on the variation throughout the inner crust of the pressure P and the following four compositional parameter: with $n_{\rm n}$ the local free neutron density and $n_{\rm b}$ the overall baryon density of matter,

- $v$, the volume fraction of clustered matter (the component which contains the protons),
- $X_{\rm n}$, the density fraction of free neutrons, $X_{\rm n} = (1-v)n_{\rm n}/n_{\rm b}$,
- $r_{\rm C}$, the radius of the WS cell, and
- $x$, the *local* proton fraction of clustered matter.

Any other compositional quantities can be expressed in terms of these four; for example, the mass and charge number of nuclei $A = 4\pi r_{\rm C}^3(1-X_{\rm n})/3$, $Z = xA$ over the range where spherical nuclei exist (it is not defined for the pasta phases as the nuclear clusters are not localized to one WS cell).

In Fig. 5 we show the variation of the crust-core and spherical nuclei-pasta transition densities and pressures over the range of $L$. Results are plotted for EoSs using the PNM low constraint and also constant $J = 25$, 30, 35 MeV. For the crust-core transition we also show results for the PNM high constraint for reference.

Whether we choose the PNM constraint or constant $J$ constraint, the crust-core transition density shows the expected negative correlation with $L$, although for the PNM constraint the correlation is much less pronounced; for PNM low, $n_{\rm cc} \approx 0.07 - 0.095$ fm$^{-3}$, a variation of 0.25 fm$^{-3}$; for constant $J = 35$ MeV $n_{\rm cc} \approx 0.05 - 0.012$ fm$^{-3}$, a variation of 0.07 fm$^{-3}$. The crust-core transition density also clearly depends on $J$ with a positive correlation, and a variation of $\approx 0.3$ fm$^{-3}$ from $J = 25 - 35$ MeV independent of $L$; a higher symmetry energy favors a larger proton fraction in the nuclear clusters, lowering their bulk binding energy to a greater extent than the increase in symmetry energy, thereby making the clustered matter energetically favorable to higher densities. For the 'PNM' sequence, $J$ increases with $L$, and so the decrease of the transition density with $L$ is compensated slightly by the increase of the transition density with $J$, making the $n_{\rm cc} - L$ correlation shallower. Indeed, with a sufficiently steep correlation between $J$ and $L$, the correlation can vanish or even be reversed; if we were to take the HVH correlation of Fig. 2, we would see no correlation between $n_{\rm cc}$, and $L$. The shaded region, consistent with experiment and the SP constraint, encompasses crust-core transition densities of $0.08 - 0.12$ fm$^{-3}$.

Relative to the crust-core transition density, the spherical nuclei-pasta transition density shows very little variation with $L$ and $J$, tracing out a thin band $n_{\rm p} \approx 0.05 - 0.06$ fm$^{-3}$.

The transition pressures show very different correlations with $L$ depending on whether we choose the PNM constraint (positive correlation) or the constant $J$ constraint (negative correlation). However, it can be seen that transition pressure has a positive correlation with $J$; for the PNM constraint J increases with L, and so overall the correlation is determined by the competition between increasing $P_{\rm cc}$ with $J$ and decreasing $P_{\rm cc}$ with $L$. The spherical-pasta transition pressure $P_{\rm p}$ also increases with $L$ for the PNM constraint, whereas the variation with $L$ at constant $J$ varies more weakly with $L$ with the same dependence, phenomenologically, as the transition density.

The crust-core and spherical-pasta transition pressures consistent with PNM low and $25 < J < 35$ MeV both vary by more than a factor of 2, $P_{\rm cc} \approx 0.35 - 0.85$ MeV fm$^{-3}$, $P_{\rm p} \approx 0.15 - 0.3$ MeV fm$^{-3}$.

Note that the shaded region is bounded by the 'PNM' and 'J35' sequences for $L < 70$ MeV; these two sequences will be taken as the bounding regions in what follows.

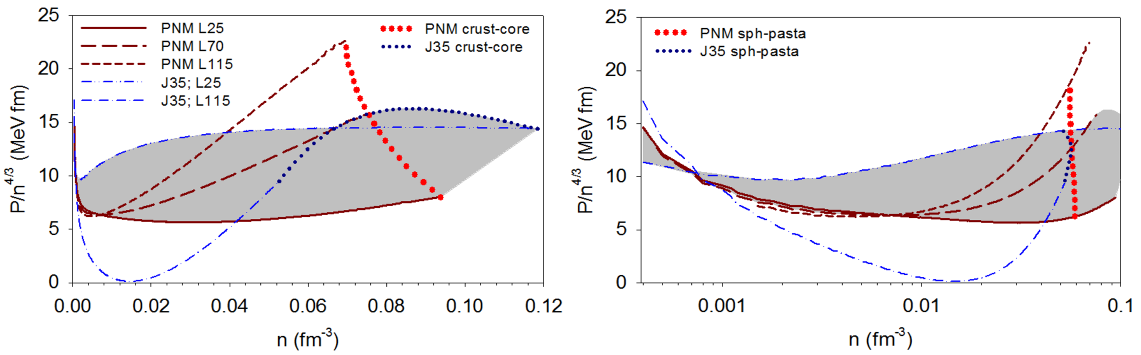

FIG. 6: (Color online) Pressure of matter scaled by $n^{4/3}$ versus baryon number density in the inner crust. Results are displayed for the $L = 25, 70$ and 115 MeV members of the 'J35' and 'PNM' sequences. The left panel displays the results over the whole density range of the inner crust, while the right panel shows the lower density region up to the transition to pasta. The loci of the transition densities over the range $L = 25 - 115$ MeV are displayed for the 'PNMlow' sequence (larger black circles) and the 'J35' sequence (smaller blue circles). The shaded region has the same meaning as in Fig. 5.

We now look at the ranges of compositional parameters predicted in the baseline model. Results are shown for the 'PNM' and 'J35' sequences for $L = 25, 70$ and 115 MeV. Note that the two sequences coincide at $L = 70$ MeV. The left panels show the full density range on a linear scale, which emphasizes the values within the range of the pasta phases. The loci of the crust-core transition densities are shown for both PNM low (larger black circles) and constant $J$ (smaller blue circles). The right panels show the range of densities up to the transition to pasta; when the predictions using the different $L$ and $J$ values differ significantly at the lower densities, a logarithmic scale is used to clearly display those differences. The loci of the spherical-pasta transition densities are shown for both PNM low (larger black circles) and constant $J$ (smaller blue circles).

Fig. 6 shows the total pressure of matter throughout the crust, scaled to $n^{4/3}$; a free, relativistic neutron gas would result in a constant. Most models, throughout the middle regions of the inner crust, predict a roughly constant trend too. The main deviation comes from $J = 35$ MeV, $L = 115$ MeV, values which predict the slope for PNM energy per particle versus density, and hence the pressure of PNM, to approach zero at low densities. As expected, since the pressure comes to be dominated by the free neutrons in the crust, a

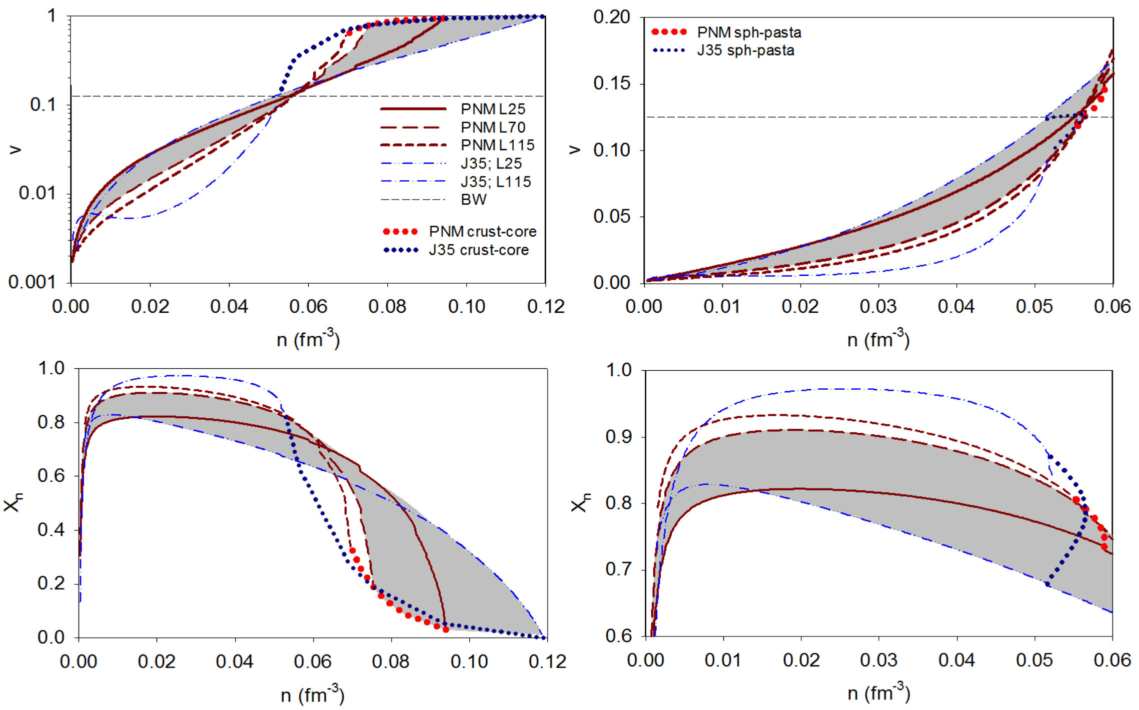

FIG. 7: (Color online) The volume fraction $v$ occupied by nuclei/nuclear clusters (top), and density fraction $X_{\rm n}$ occupied by free neutrons (bottom), versus baryon number density in the crust. The same selection of EoSs from Fig. 6 is used, and the transition loci are displayed in the same way. The shaded region has the same meaning as in Fig. 5. The left panels display the results over the whole density range of the inner crust, while the right panels show the lower density region up to the transition to pasta.

higher value of $L$ leads to a higher pressure throughout most of the crust.

Fig. 7 shows the volume fraction of clustered matter and the density fraction $X_{\rm n}$ of free neutrons. The first thing to note is that the volume fraction reaches $> 0.8$ at the crust-core transition for the shaded region; this emphasizes the fact that the WS approximation is certainly not valid at the highest crustal densities. For the PNM constraint, the crust-core transition fraction weakly depends on $L$, ranging from 0.8 ($L$=115 MeV) to close to 1.0 ($L$=25 MeV). For $J = 35$ MeV, the crust-core transition fraction varies much more widely, from close to 1 ($L$=25 MeV) down to 0.1 ($L$=115 MeV). The spherical-pasta transition fractions vary over a much smaller range from $\approx 0.11$ - 0.14 for PNM low and $\approx 0.08$ - 0.12 for $J = 35$ MeV. A useful comparison is with the simple estimate from the Bohr-Wheeler fission instability criterion (see, e.g. [80]) of 0.125, a value which closely matches the range predicted

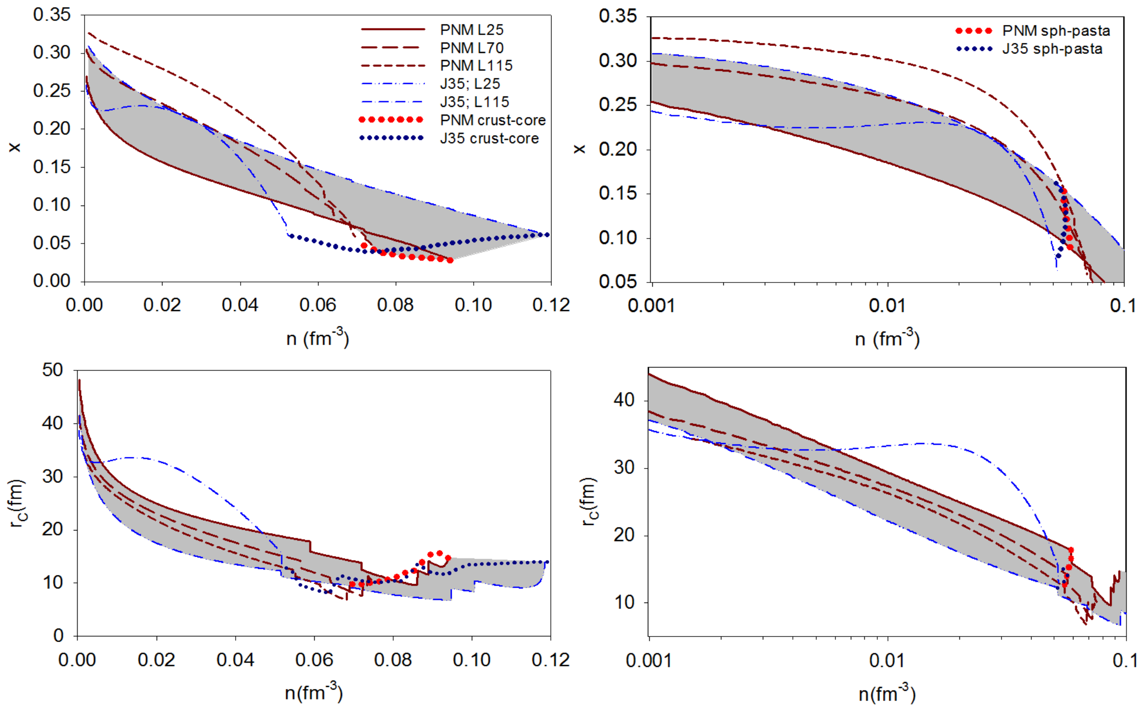

FIG. 8: (Color online) Local proton fraction of clusters $x$ (top) and WS cell size $r_{\rm C}$ (bottom) versus baryon number density in the crust. The same selection of EoSs from Fig. 6 is used, and the transition loci are displayed in the same way. The shaded region has the same meaning as in Fig. 5. The left panels display the results over the whole density range of the inner crust, while the right panels show the lower density region up to the transition to pasta.

by our baseline model. This value is indicated on Fig. 7 by the horizontal line. Below that density, the fraction varies by up to 0.05 from $L$=115 MeV (lower values) to $L = 25$ MeV (higher fractions), an easily understood correlation: higher $L$ implies higher neutron matter pressure at saturation density and below, resulting in the pressure equilibrium condition favoring smaller nuclei.

Mirroring the volume fraction at the crust-core transition, $X_{\rm n}$ varies from close to 0.0 up to 0.2. The fraction rapidly converges to zero at low densities as the density of free neutrons vanishes. $X_{\rm n}$ peaks around 0.01 - 0.03 fm$^{-3}$ with values between 0.8 - 9.6, with higher $L$ being correlated higher $X_{\rm n}$. The transition to pasta occurs close to the peak value of $X_{\rm n}$ for all $L$ and $J$.

Fig. 8 shows the cell size $r_{\rm C}$ and the proton fraction of clustered matter $x$. $r_{\rm C}$ varies smoothly up to the transition to pasta, and then proceeds through a series of discontinuous jumps as matter transitions through the various nuclear shapes. In practice, these jumps may be smoothed out by the existence of intermediate shapes not considered in this work [81]. The negative correlation with $L$ is again explained by the pressure equilibrium condition. In the right panel, it can be seen that the variation of $r_{\mathrm{C}}$ over the density range up to the transition to pasta consistent with our PNM and constant $J$ constraints is constant at $\approx 8$ fm.

$x$ generally decreases with increasing density over the whole density range. For $J = 35$ MeV, the crust-core transition fraction varies by about 0.03; from $L = 25$ MeV, $x_{\mathrm{cc}}$ decreases from 0.06 down to 0.03 at $L = 70$ MeV, then increasing back up to 0.06 at $L = 115$ MeV; for PNM the variation is similar, starting at $x_{\mathrm{cc}}$=0.025 for $L = 25$ MeV and increasing with $L$ up to 0.06 at $L = 115$ MeV. In the lower density region the variation in $x$ remains approximately constant at around 0.05. At a given density, higher $J$ and higher $L$ correlate with higher $x$. Higher $J$ favors a higher proton fraction; higher $L$ favors smaller, denser nuclei and nuclear clusters; as the symmetry energy increases with density, denser nuclei will also tend to favor higher $x$.

## VI. SURFACE ENERGY DEPENDENCE

Having established how the crustal parameters behave in our baseline sequences, we begin to examine how those results depend on the various other model parameters, starting with the surface and curvature parameters. In the following figures, the baseline results will be represented as the shaded regions, bounded by the 'PNM' and 'J35' sequences and $L < 70$ MeV.

In this section we consider the same set of transition and compositional parameters as in the previous section. We examine changes in the behavior of the surface and curvature energies at proton fractions near 0.5 (as controlled by the surface symmetry parameter $\sigma_{\delta}$ through the correlation with the bulk symmetry energy $J$, controlled by the parameter $c$) and low proton fraction, as controlled by the parameter $p$. We vary $c$ from 2.0 to 7.0 (which, for any given value of $J$ corresponds to an increase in $\sigma_{\delta}$ by a factor of 3.5); note, a higher value of $c$, and therefore $\sigma_{\delta}$, gives a *lower* surface energy at a given proton fraction $X$. We also examine the cases of $p = 2$ and $p = 4$ as mentioned in section IV.A. $p = 2$ gives a substantially higher surface energy at low proton fractions, while $p = 4$ is substantially

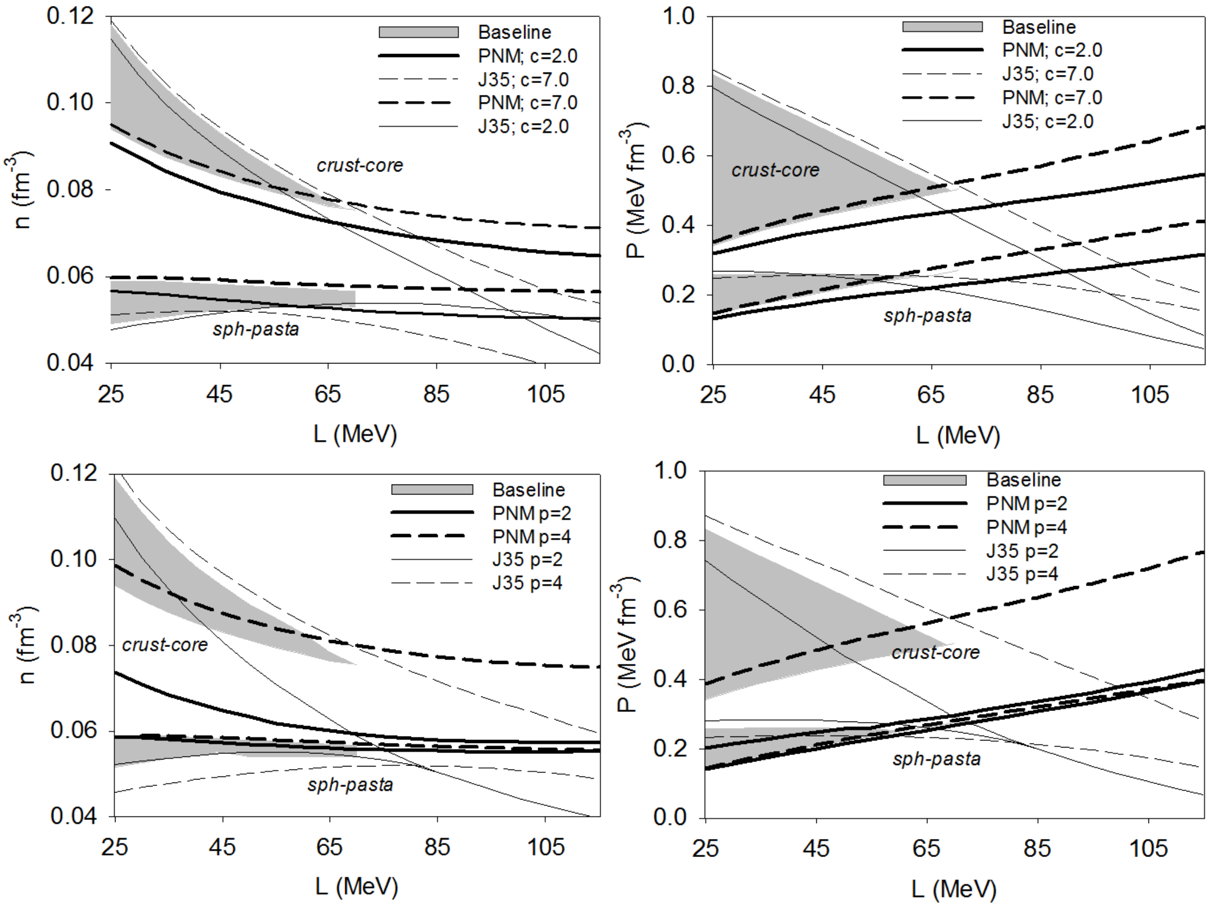

FIG. 9: Crust-core and spherical nuclei-pasta transition densities (left) and pressures (right) versus $L$ for the 'PNM' (thick lines) and 'J35' (thin lines) sequences. The top two plots show the results with $c = 2.0$ (solid lines) and $c = 7.0$ (dashed lines); the bottom two plots show the results with $p = 2$ (solid lines) and $p = 4$ (dashed lines). The baseline results are shown for reference as the shaded regions.

lower (see Fig. 4).

Fig. 9 displays the transition densities and pressures. The top two figures show the 'PNM' and 'J35' sequences with $c = 2.0$ and $c = 7.0$; the lower two figures show the two sequences for $p = 2.0$ and $p = 4.0$. A higher surface and curvature energy will tend to favor a lower transition density, as the energy cost of having a surface is higher; for a given value of $L$ on any of the sequences, we would thus also expect a higher transition pressure. This trend should be the opposite for the spherical nuclei-pasta transition; the pasta shapes generally have a larger surface, so a higher surface energy would favor the spherical nuclei to higher

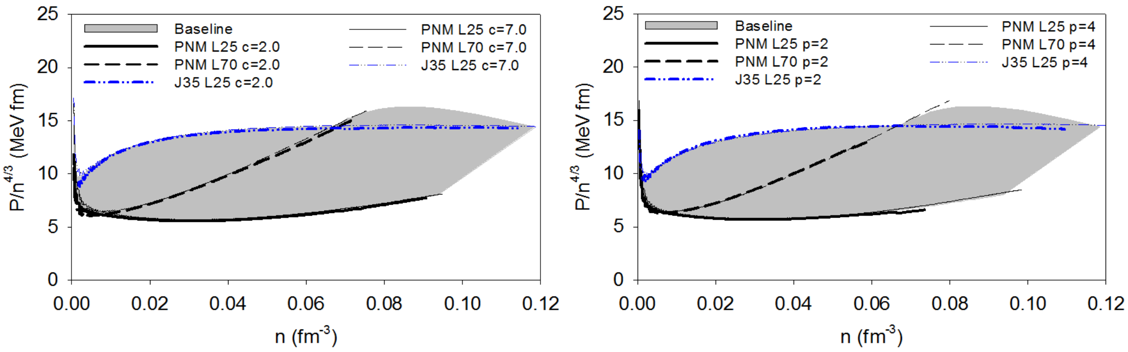

FIG. 10: (Color online) Pressure of matter scaled by $n^{4/3}$ versus baryon number density in the inner crust. Results are displayed for the $L = 25$ and 70 MeV members of the 'J35' and 'PNM' sequences. The left panel displays the results at $c = 2$ and $c = 7$; the right panel for $p = 2$ and $p = 4$. The baseline region is shown for reference.

densities. Thus a higher surface energy decreases the density range over which pasta nuclei are energetically favorable.

This is indeed what we see; the $c = 2.0$, $p = 2$ sequences have lower crust-core transition densities and higher spherical-pasta transition densities compared to the baseline ($c = 4.8$) results, while the $c = 7.0$, $p = 4$ sequences have elevated crust-core transition densities, and lower spherical-pasta transition densities.

The effect on the transition densities is relatively small when $c$ is varied, amounting to $\approx 0.005$ fm$^{-3}$ around the baseline results for the most part. The variation with $p$ is more dramatic; for $p = 4$ the difference with the baseline results is still relatively small ($< 0.005$ fm$^{-3}$) but for $p = 2$ the crust-core transition density is significantly lower then the baseline results, falling by 0.02 fm$^{-3}$ throughout the 'PNM' sequence, and by up to that amount for the 'J35' sequence at high $L$. The effect on the spherical nuclei-pasta transition is not as dramatic; the end result is that the region in which the pasta shapes are present is significantly reduced; the corresponding effect on macroscopic crust properties is discussed in section IX.

For the compositional parameters throughout the inner crust, we display results for the $L = 25$ MeV and $L = 70$ MeV members of the 'J35' and 'PNM' sequences, which together bound the shaded regions for the baseline results. Fig. 10 shows the pressure scaled by $n^{4/3}$, Fig. 11 shows the volume fraction $v$ and density fraction $X_{\rm n}$ occupied by free neutrons, and

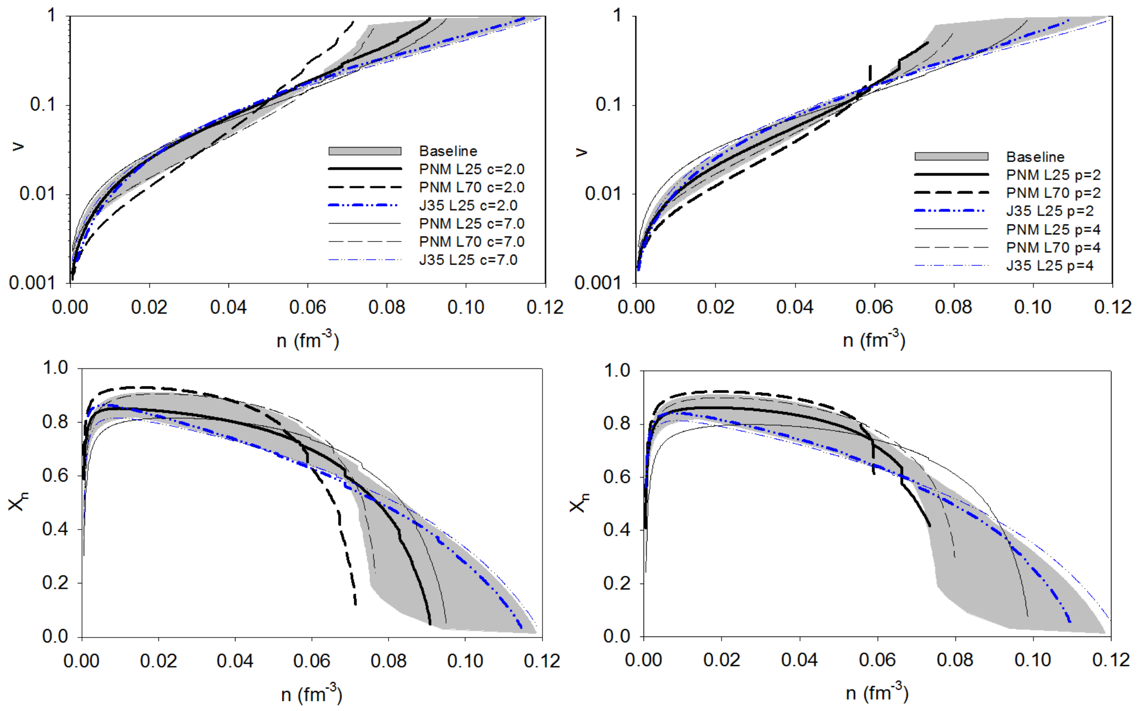

FIG. 11: (Color online) The volume fraction $v$ occupied by nuclei/nuclear clusters (top), and density fraction $X_{\rm n}$ occupied by free neutrons (bottom), versus baryon number density in the crust. Results are displayed for the $L = 25$ and 70 MeV members of the 'J35' and 'PNM' sequences. The left panel displays the results at $c = 2$ and $c = 7$; the right panel for $p = 2$ and $p = 4$. The baseline region is shown for reference.

Fig. 12 the local proton fraction of clusters $x$ (top) and WS cell size $r_{\rm C}$; in each case the baseline results (shaded regions) are compared with the upper and lower limits of the surface - bulk symmetry correlation $c = 2.0, 7.0$ (left hand panels) and the low-proton fraction surface parameter $p = 2, 4$. The pressure exhibits very little dependence on either of the surface parameters, dominated as it is by the pressure of the dripped neutrons. The volume fraction shows little dependence on $c$ throughout most of the crust; at higher densities it reaches the same maximum values as the baseline at a slightly lower (higher) density for $c$=2.0 (7.0). Throughout most of the crust, $p$ has little effect on the volume fraction; however, just as $p$=2 gives a large reduction in the transition density and pressure, the volume fraction is also reduced significantly, down to about 0.3, reflecting the fact that the increased surface energy becomes prohibitive when the clusters occupy a much smaller fraction of the space. The free neutron fraction exhibits the same dependence on $c$ and $p$, with a significant effect

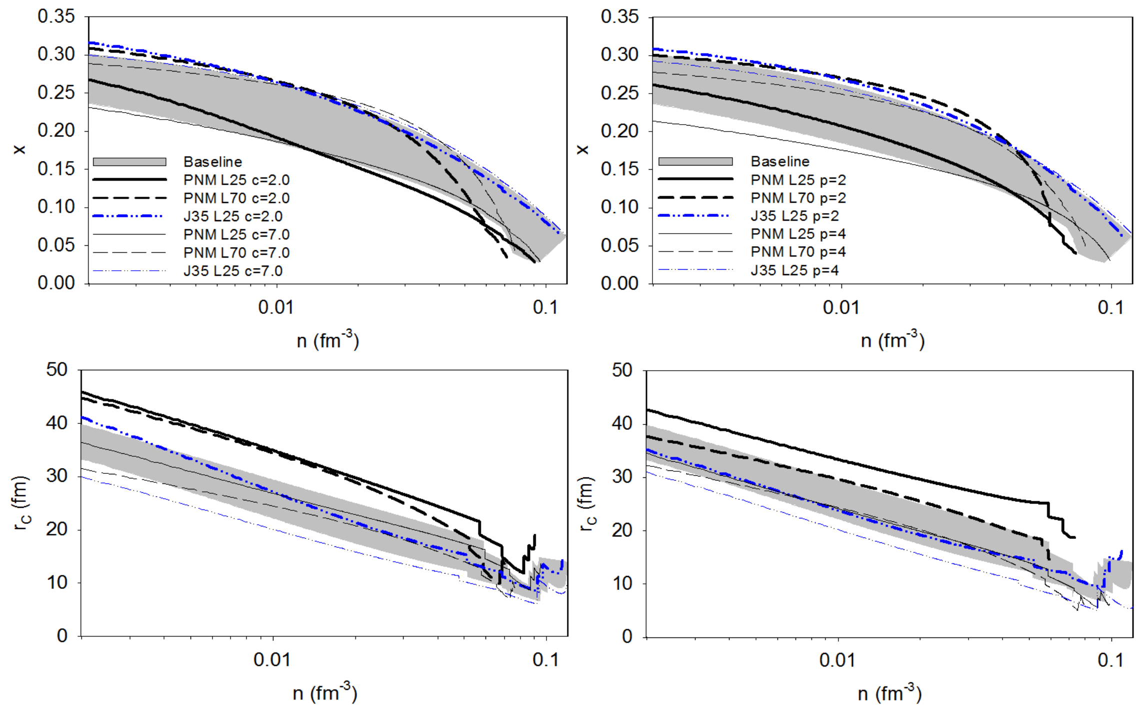

FIG. 12: (Color online) Local proton fraction of clusters $x$ (top) and WS cell size $r_{\mathrm{C}}$ (bottom) versus baryon number density in the crust. Results are displayed for the $L = 25$ and 70 MeV members of the 'J35' and 'PNM' sequences. The left panel displays the results at $c = 2$ and $c = 7$; the right panel for $p = 2$ and $p = 4$. The baseline region is shown for reference.

only for $p$=2.

Similarly, $c$ and $p$ have relatively little effect on the proton fraction throughout most of the crust; a lower value of $c$ or $p$ (higher surface energy at high and low proton fractions) is associated with a marginally higher proton fraction at lower densities, as an increased proton fraction lowers the energy of the bulk matter inside the nuclei (makes it more bound) to compensate for the increased surface energy. In contrast, the size of the WS cell does exhibit a significant dependence on the surface parameters, shifting the baseline sizes on the order of 5 fm higher (lower) for lower (higher) values of $c$ and $p$ throughout most of the inner crust. Since the volume fractions are relatively unchanged, this means that the nuclear sizes are also higher (lower). This can be understood from the competition between the surface and bulk energies: raising the surface energy (by lowering $c$ or $p$) can be compensated by increasing the contribution to the total energy density of the bulk phases of matter relative to the surface contribution.

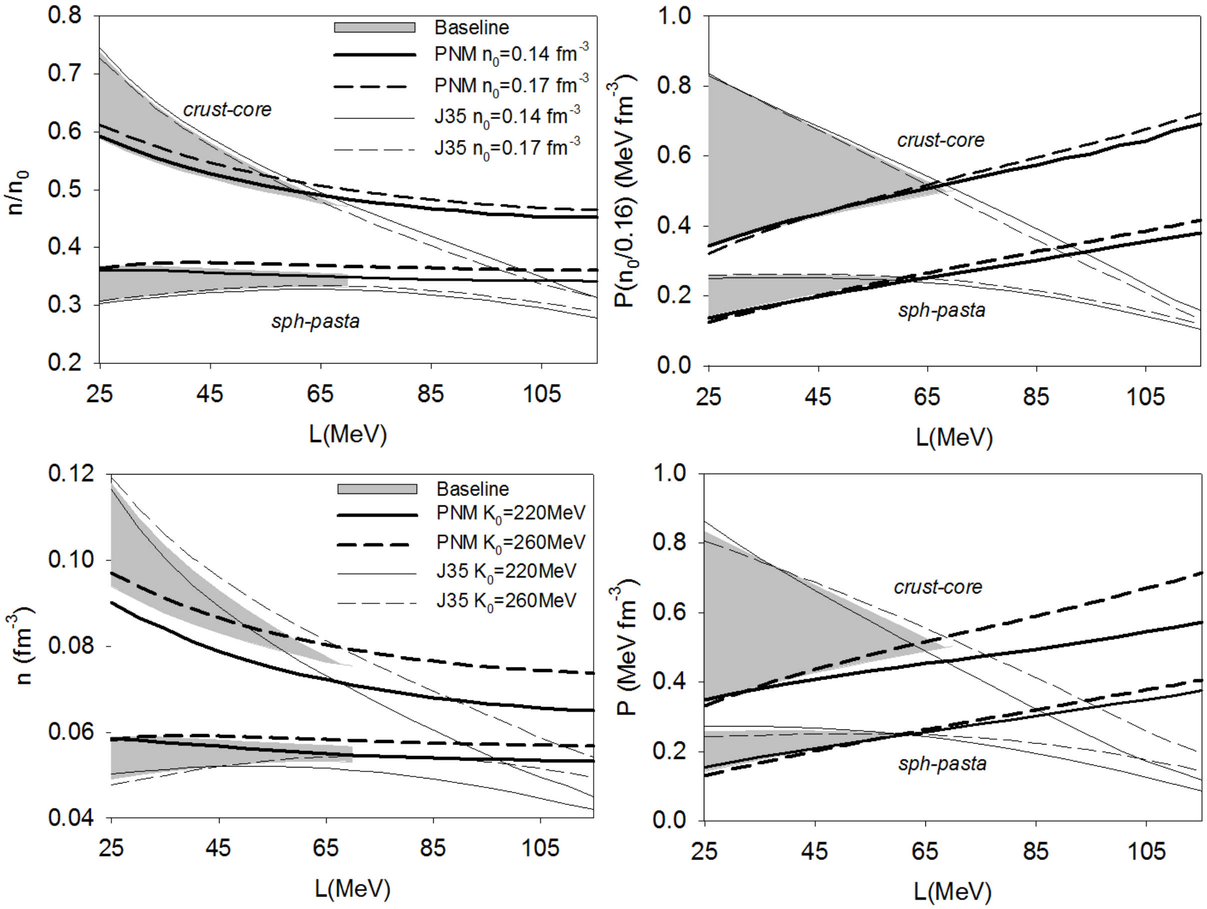

FIG. 13: Crust-core and spherical nuclei-pasta transition densities (left) and pressures (right) versus $L$ for the 'PNM' (thick lines) and 'J35' (thin lines) sequences. The top plots show the results for the saturation densities $n_0 = 0.14$ fm$^{-3}$ (solid lines) and $n_0 = 0.17$ fm$^{-3}$ (dashed lines), with the densities and pressures scaled to $n_0$; the bottom two plots show the results with $K_0 = 220$ MeV (solid lines) and $K_0 = 260$ MeV (dashed lines). The baseline results are shown for reference as the shaded regions.

## VII. DEPENDENCE ON INCOMPRESSIBILITY AND SATURATION DENSITY OF NUCLEAR MATTER

We now examine the impact on the transition properties and composition of varying the properties of SNM at saturation densities via the incompressibility $K_0$ and saturation density $n_0$ within experimentally constrained values, relative to our baseline results. The ranges of variation used are 220< $K_0$ <260 MeV and 0.14< $n_0$ <0.17 fm$^{-3}$.

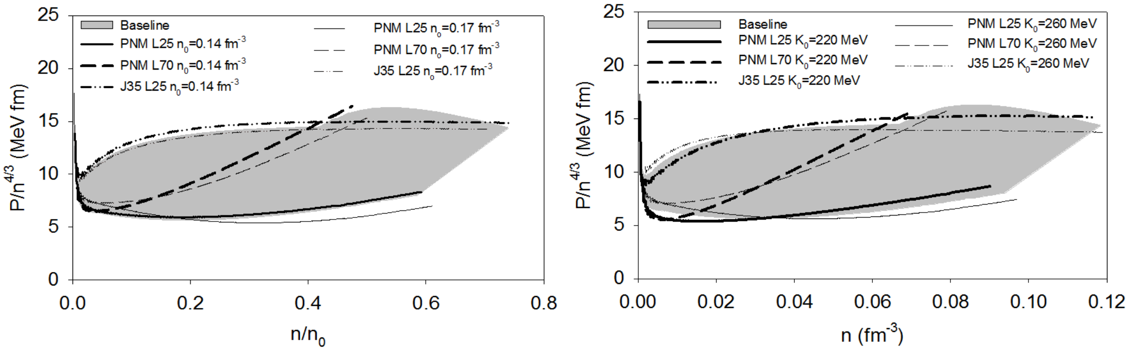

FIG. 14: Pressure of matter scaled by $n^{4/3}$ versus baryon number density in the inner crust. Results are displayed for the $L = 25$ and 70 MeV members of the 'J35' and 'PNM' sequences. We show results for $n_0 = 0.14(0.17)$ fm$^{-3}$ (thick, (thin) lines) versus density scaled to $n_0$ in left panels and $K_0 = 220(260)$ MeV (thick (thin) lines) in the right panels. The baseline region is shown for reference.

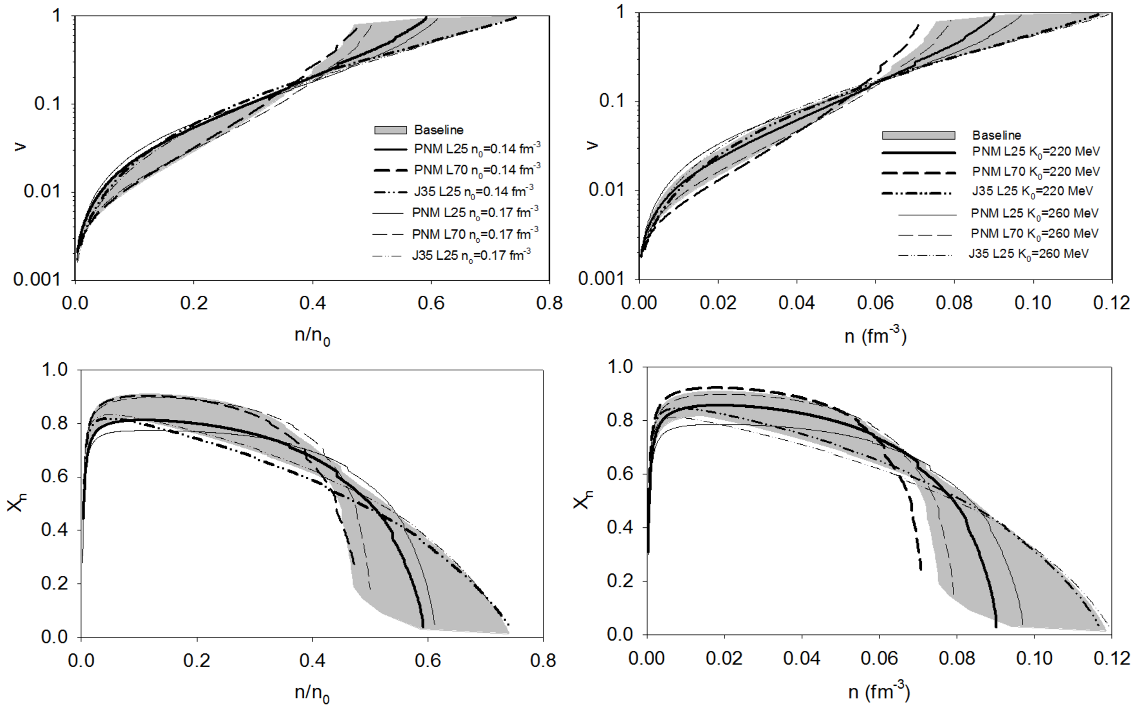

FIG. 15: The volume fraction $v$ occupied by nuclei/nuclear clusters (top), and density fraction $X_{\rm n}$ occupied by free neutrons (bottom), versus baryon number density in the crust. $n_0(K_0)$ are in the left (right) panels in the same way as Fig. 14.

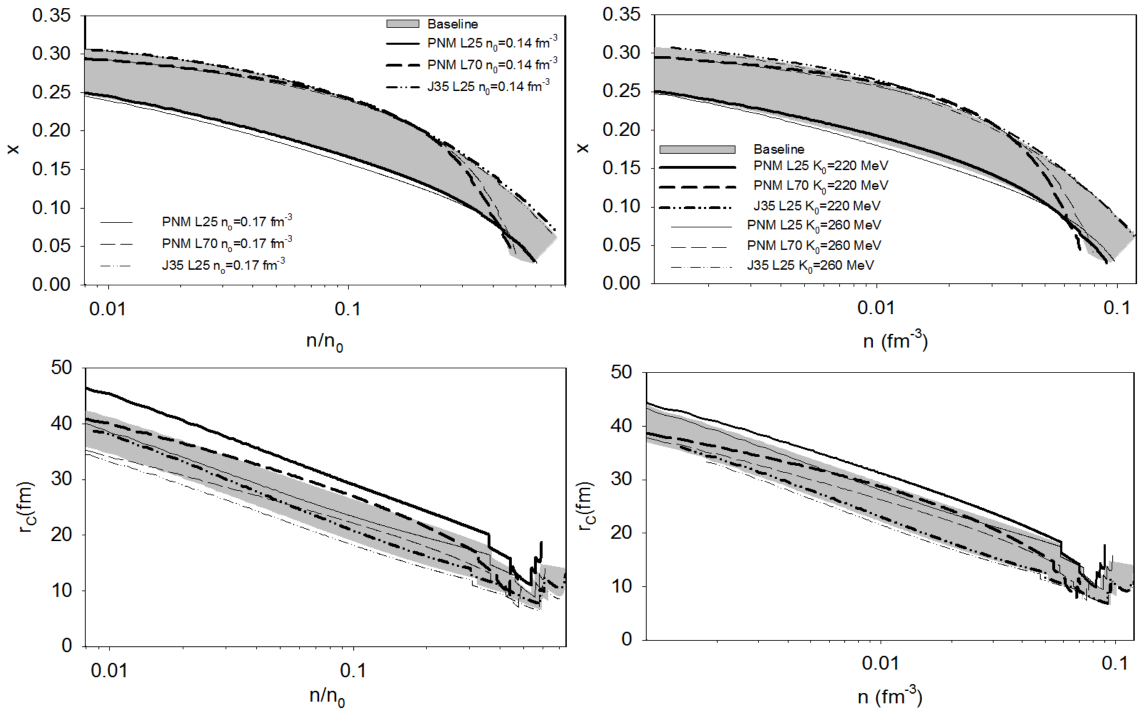

FIG. 16: Local proton fraction of clusters $x$ (top) and WS cell size $r_C$ (bottom) versus baryon number density in the crust. The left and right panels show the results for the variation in $n_0$ and $K_0$ in the same way as Fig. 14.

Decreasing (increasing) $K_0$ and $n_0$ results in a decrease (increase) in the crust-core transition density and pressure. In Fig. 13 we plot the transition densities (left) and pressures (right) versus $L$ for $n_0 = 0.14, 0.17$ fm$^{-3}$ (top two plots) and $K_0 = 220, 260$ MeV (bottom two plots), for the 'PNM' and 'J35' sequences. Results are compared with the baseline results (shaded area).

Varying $n_0$ simply rescales the EoS; we thus plot the transition densities and pressures scaled to the new saturation density in the top two plots. Plotted in this way, $n_{\rm cc}$ and $P_{\rm cc}$ show little variation from the baseline results, indicating that, to good accuracy, the saturation density simply rescales them linearly. The lower (higher) $K_0$ values give lower (higher) values for $n_{\rm cc}$ and $n_{\rm p}$ by up to $\approx 0.005$ fm$^{-3}$; for the transition to pasta the effect is greatest at high $L$. Similarly, the pressures are lowered (raised) for lower (higher) $K_0$; the effect is greater at high $L$, up to $\approx 0.005$ fm$^{-3}$ for $P_{\rm cc}$; the effect on the pasta transition is small.

In Figs. 14-16 we show the effect from the variation of $K_0$ and $n_0$ on the pressure and composition throughout the crust. Again, when examining the effect of the saturation density, we scale the crust density by $n_0$. $P/n^{4/3}$ shows little variation with $n_0$ (once the density is rescaled) and $K_0$; although equation 13 shows a first-order dependence on $K_0$, its variation is much smaller than that of $L$. $v$ and $X_{\rm n}$ show a very small dependence for the same reason, as they are largely determined by the symmetry energy and pressure. Similarly $x$, determined in large part by the symmetry energy at a given density, shows negligible dependence. The WS cell size $r_{\rm C}$ is the only parameter to show a significant dependence, increased by $\approx 5$ fm relative to the baseline results by lowering the saturation density.

## VIII. DEPENDENCE ON EOS

So far we have examined the dependence of crustal composition on the properties of the EoS at saturation density $L, K_0$ and $n_0$ while fixing the absolute value of the energy of PNM either at saturation density (by keeping $J$ constant) or at very low densities (the PNM constraint). However, as Fig. 1 shows, this still allows some freedom of the PNM EoS at intermediate densities; for example, the MSL and BD EoSs, constrained by the same low density EoS, differ significantly at intermediate densities, the BD EoS giving a lower energy of PNM (and therefore pressure) for a given value of $L$, a fact that shows up in the difference in the correlations obtained in Fig. 2. We now examine the effect of these differences.

In Fig. 17 the crust-core transition densities and pressures are shown for the 'PNM' and 'J35' sequences of the BD EoS, as well as for the Skyrmes listed in Table 1, compared to our baseline MSL results. For the BD EoSs, the baseline quantities in Table 2 are used; the Skyrmes use the same surface parameters, and their saturation EoS properties are given in Table 1. There is little difference between the MSL and BD baseline results for the transition densities, and the Skyrmes fall within or very close to the baseline region. The 'J35' BD sequence and the Skyrmes are also consistent with the MSL baseline results, but the 'PNM' BD sequence gives significantly lower pressures than the equivalent MSL sequence. These results are expected; the 'J35' MSL and BD EoSs match closely (Fig. 1), but as stated above, the BD EoSs give a consistently lower PNM pressure at intermediate densities than the MSL EoSs when constrained by the same low density PNM EoS. We can therefore expect any quantities that are sensitive to the pressure of the dripped neutrons will also be sensitive to

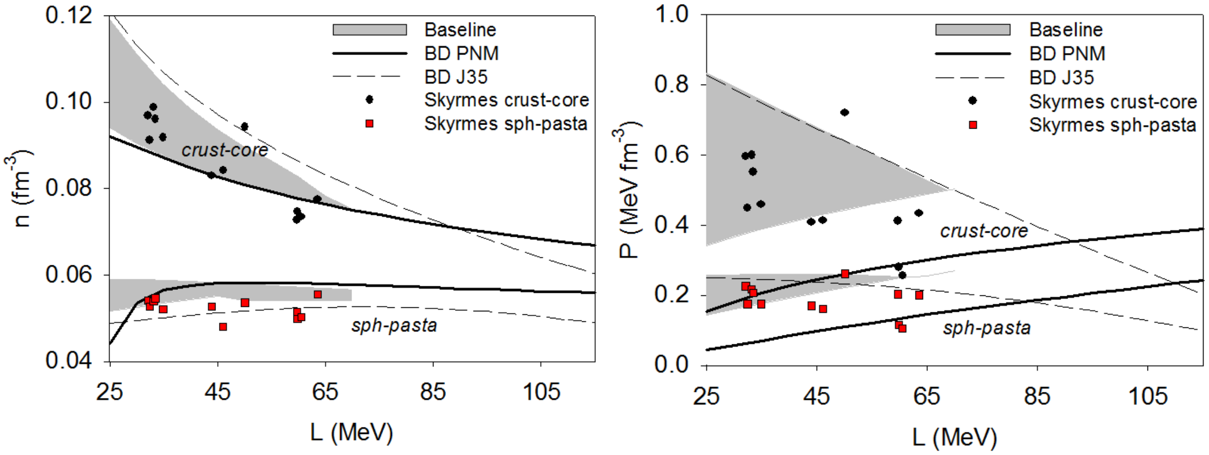

FIG. 17: (Color online) Crust-core and spherical nuclei-pasta transition densities (left) and pressures (right) versus $L$ for the 'PNM' (thick lines) and 'J35' (thin lines) sequences of the BD EoS, together with the selection of Skyrmes. The baseline results are shown for reference as the shaded regions.

these differences in the EoS.

This is exemplified in Fig. 18, where the pressure scaled by $n^{4/3}$ is plotted for the BD EoSs on the left and for a selection of Skyrmes on the right. In this figure, and Figs. 19-20, we plot both the $L = 25, 70$ MeV members of the J35 and PNM sequences, the same members that

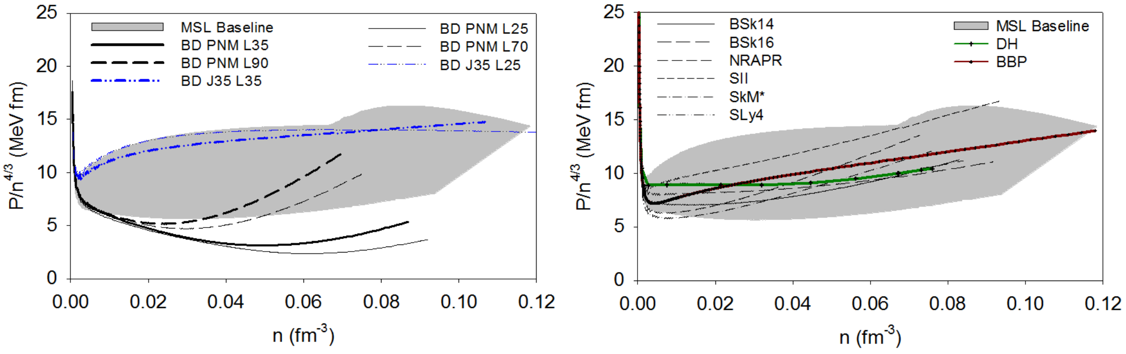

FIG. 18: (Color online) Pressure of matter scaled by $n^{4/3}$ versus baryon number density in the inner crust. On the left the results of the BD EoS are displayed for the $L = 25, 35$ and $70, 90$ MeV members of the 'J35' and 'PNM' sequences. The right panel displays the results for our selection of Skyrmes together with the DH EoS [38] (DH) and BBP [29] EoSs. The baseline region is shown for reference.

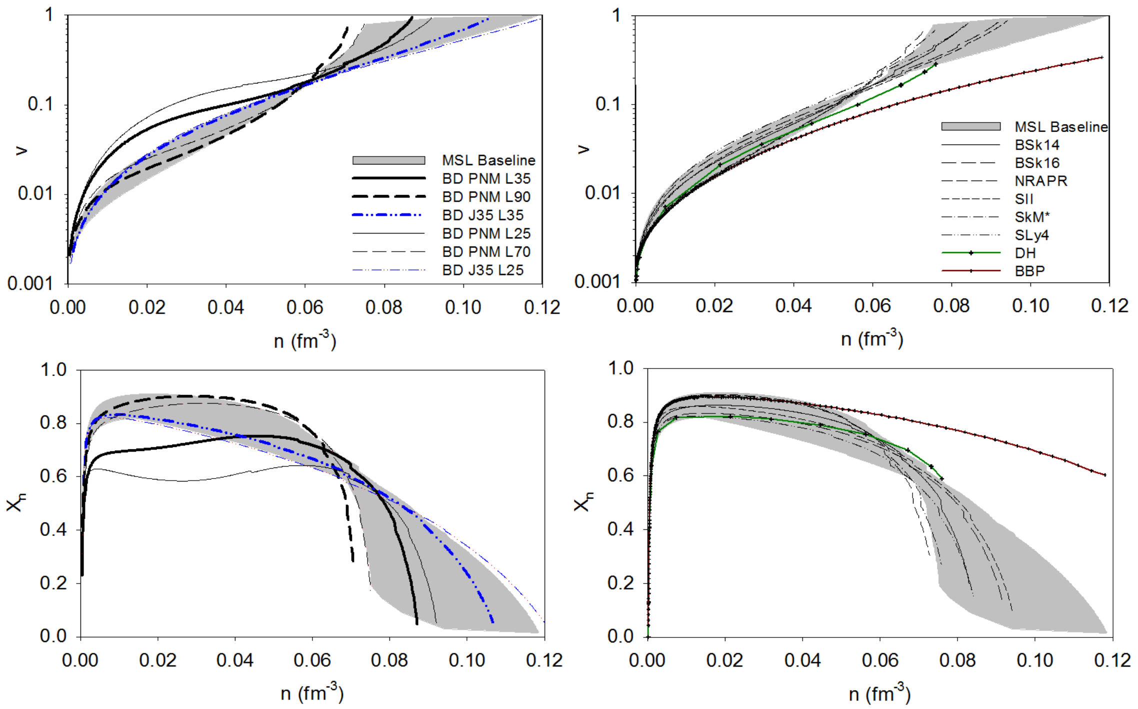

FIG. 19: (Color online) The volume fraction $v$ occupied by nuclei/nuclear clusters (top), and density fraction $X_{\mathrm{n}}$ occupied by free neutrons (bottom), versus baryon number density in the crust. The EoSs displayed in the left and right hand panels are the same as Fig. 18.

largely determine the shaded bounds from the MSL baseline models, and also the $L = 35, 90$ MeV members of the same sequences; these bound the set of BD EoSs that are consistent with the PNM constraints and $25 < J < 35$ MeV. The BD EoSs match the MSL EoSs for the low density part of the inner crust, up to $n \approx 0.02$ fm$^{-3}$ before diverging significantly in the high density region, with the pressure from the BD EoSs being lower, especially for lower values of $L$. However, the Skyrmes used all fall within the baseline region. We also plot here, and in Figs. 19-20, the results from the widely used Douchin and Haensel [38] (DH) and Baym, Bethe, Pethick [29] (BBP) EoSs, both of which have pressures within the baseline region.

In Fig. 19, $v$ and $X_{\mathrm{n}}$ are plotted versus density for the BD EoSs (left) and the Skyrme EoSs together with DH and BBP (right). These quantities are also sensitive to the pressure of PNM over the whole density range up to saturation; a lower PNM pressure gives rise to nuclei occupying a larger fraction of the space (higher $v$) and thus a lower density fraction of dripped neutrons, which is what we see for most of the crust. Again, the Skyrmes tested are

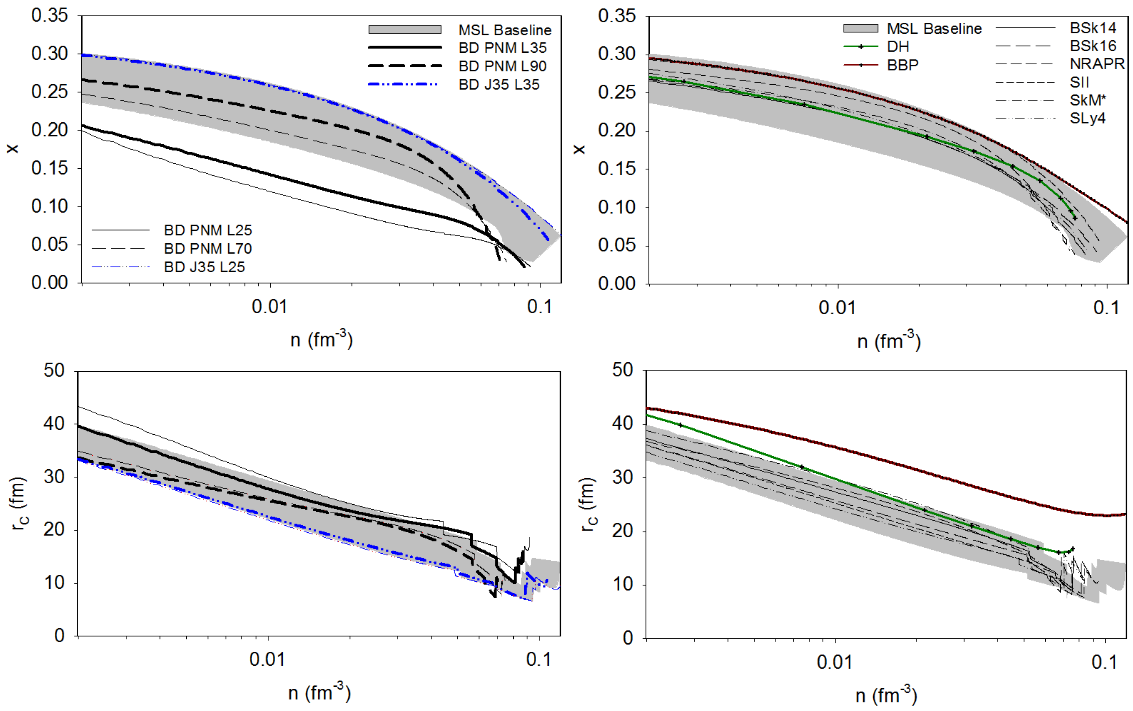

FIG. 20: (Color online) Local proton fraction of clusters $x$ (top) and WS cell size $r_{\rm C}$ (bottom) versus baryon number density in the crust. The EoSs displayed in the left and right hand panels are the same as Fig. 18.

consistent with the baseline results. The DH EoS is also consistent, but the BBP EoS gives a much lower volume fraction and consequently much higher dripped neutron density fraction over the higher density region of the crust. This results from the high compressibility $K_0$ used for the BBP EoS and an unrealistically high surface tension.

In Fig. 20, $x$ and $r_{\rm C}$ are plotted versus density for the BD EoSs (left) and the Skyrme EoSs together with DH and BBP (right). The WS cell size $r_{\rm C}$ appears insensitive to the reduced neutron pressure of the BD EoSs, while the local proton fraction $x$ drops by up to 0.05 for $L = 25, 35$ MeV; in order to reduce the lattice Coulomb energy cost of increasing the nuclear size (which happens because of the reduced dripped neutron pressure), the proton fraction drops, which will maintain a roughly constant nuclear charge number. The Skyrmes again fall within the region of the MSL baseline results. The DH EoS is also consistent although it falls at the upper boundary of the WS cell size region. The BBP EoS predicts a larger WS cell size.

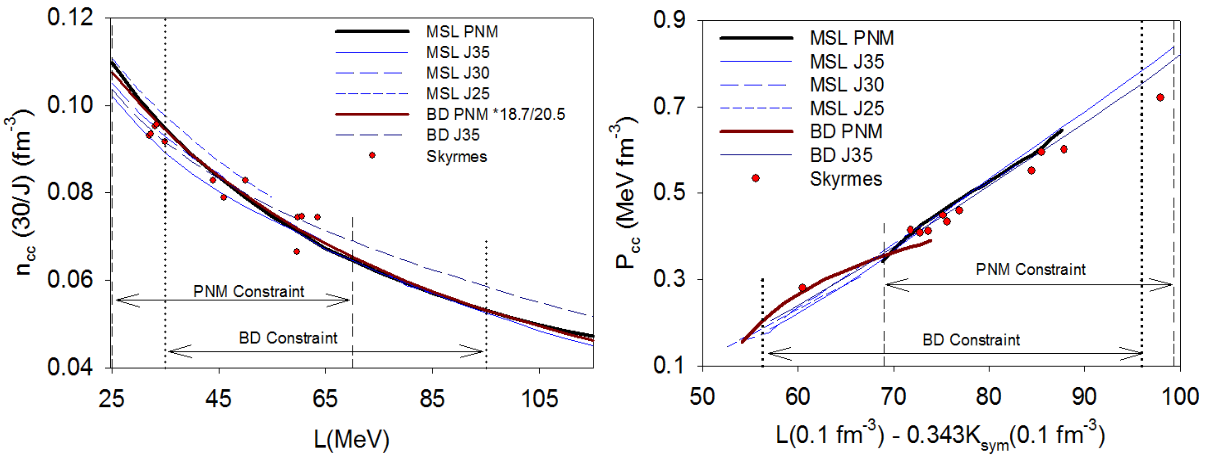

FIG. 21: (Color online) Crust-core densities scaled by 30 MeV/$J$ (left) versus $L$ and transition pressures versus $L(n = 0.1\ \mathrm{fm}^{-3})$ - 0.343 $K_{\mathrm{sym}}(n = 0.1\mathrm{fm}^{-3})$ for the 'PNM' and selected 'J' sequences of MSL and BD EoSs, and for selected Skyrmes.

## IX. DISCUSSION

The transition densities for the sequence of constant $J$ EoSs (Fig. 5) indicates a roughly inverse linear scaling of the densities with $J$. With this in mind, we plot in the left panel of Fig. 21 the transition densities multiplied by $30/J$ (using $J = 30$ MeV as a reference value). To add the 'PNM' results we must of course use the correlation of $J$ with $L$. Our Skyrme selection is also plotted. We also add onto the plot the BD EoS results; for the BD 'PNM' sequence we must also scale the density according to the offset of the correlation relative to the MSL correlation. Once this is done, the results form a relatively tight band correlated with $L$.

It was suggested that a tighter correlation would be obtained by plotting $P_{\mathrm{cc}}$ against some combination of EoS parameters rather than just $L$ [14]; an optimum fit was obtained for $L(n = 0.1\mathrm{fm}^{-3})$ - 0.343 $K_{\mathrm{sym}}(n = 0.1\mathrm{fm}^{-3})$ using transition pressures obtained using stability analyses. Such a correlation can be understood as follows: the pressure of the matter at the crust-core transition is related to the pressure of PNM at around the same density ($\sim$ 0.1 fm$^{-3}$); equation 14 shows that this will be related, to the first two orders, with $L$ and $K_{\mathrm{sym}}$ at $n \sim 0.1$ fm$^{-3}$ when $K_0$ is fixed. We plot the same quantities obtained in our model for the 'PNM' and constant J sequences of both MSL and BD EoSs, as well as the Skyrme EoSs, on the right panel of Fig. 21. A tight correlation is indeed observed, reinforcing the

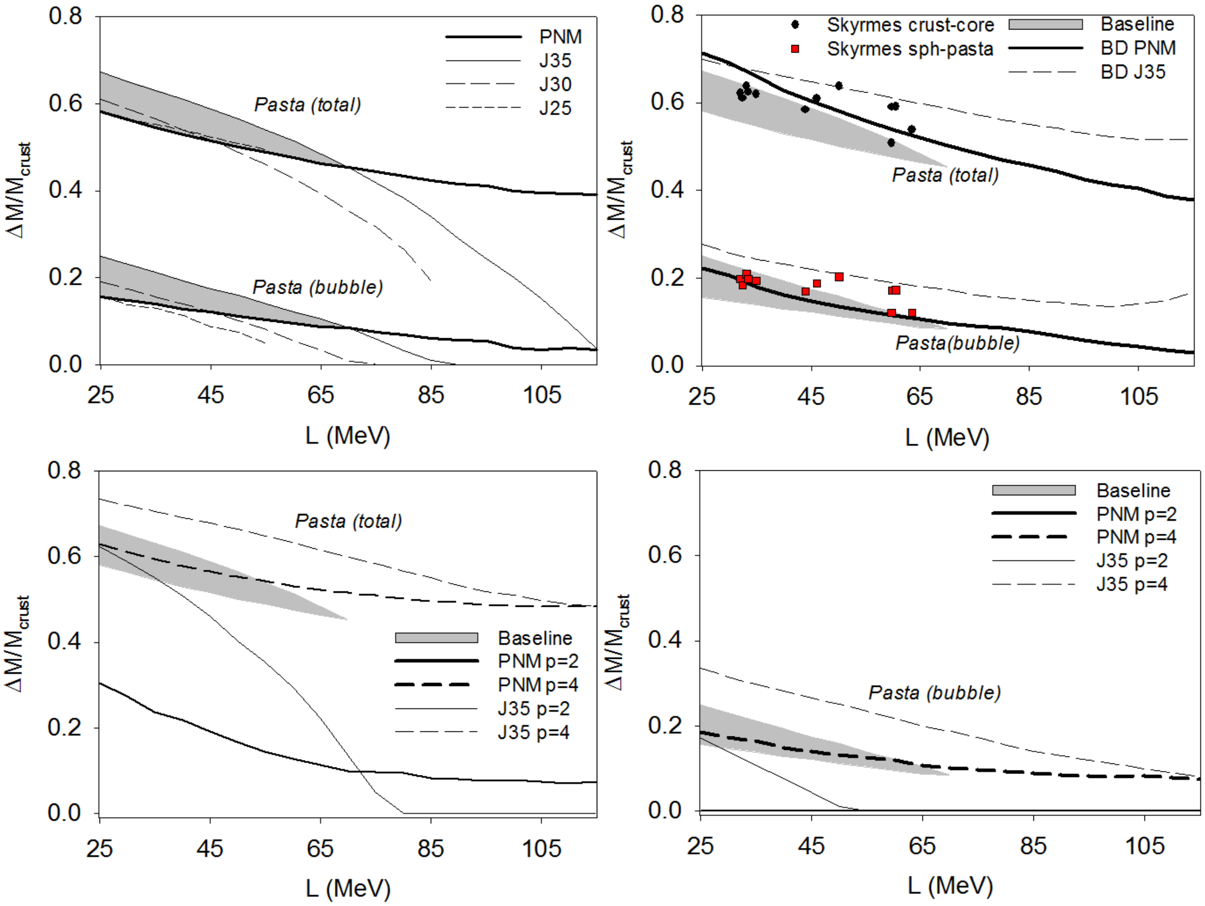

FIG. 22: Fraction of mass contained within the pasta phases as a whole and the bubble phases relative to the total crust mass versus $L$. The top left panel shows the baseline results; top right the comparison with the BD EoSs and Skyrmes; bottom left and right the variation with the surface parameter $p$.

applicability of this method, and indicating that more experimental data on the symmetry energy at sub-saturation densities, as well as experimental probes of the curvature of the symmetry energy $K_{\rm sym}$ would improve our estimate of the transition pressure.

The regions over which the MSL and BD EoSs are consistent with both the low density PNM constraint and $25 < J < 35$ MeV are depicted on the plots; these are still relatively large allowed regions. For MSL, the region spans transition densities $\approx 0.076 - 0.12$ fm$^{-3}$ and transition pressures $\approx 0.36 - 0.8$ MeV fm$^{-3}$; for BD the regions are $\approx 0.07 - 0.11$ fm$^{-3}$ and $\approx 0.2 - 0.75$ MeV fm$^{-3}$ respectively. The Skyrmes all fall within the MSL range.

The transition pressures can be used to estimate the mass and moment of inertia fractions of various components of the crust relative to the crust totals. Assuming an outer layer of the neutron star to be thin and contain relatively little mass compared to the whole star, the mass of that layer is proportional to the pressure at the base of that layer $\Delta M \propto P$ [74], otherwise depending only on the bulk properties of the star. From this, the fraction of mass contained within the pasta phases, and within only the bubble pasta phases, can be estimated as

$$\frac{\Delta M_{\rm pasta}}{\Delta M_{\rm crust}} \approx 1 - \frac{P_{\rm p}}{P_{\rm cc}}; \qquad \frac{\Delta M_{\rm bubble}}{\Delta M_{\rm crust}} \approx 1 - \frac{P_{\rm bu}}{P_{\rm cc}}. \tag{23}$$

where $P_{\rm bu}$ is the pressure of transition to the bubble phases of pasta. Since the moment of inertia contained within the various phases relative to the total crustal moment of inertia is proportional to $\Delta M$, the moment of inertia fractions will be identical to the mass fractions.

We plot the mass fractions in Fig. 22. In the top left panel, the baseline MSL results are shown. For $L < 70$ MeV, the pasta phases account for a large fraction of the mass of the crust: between 50% and 70%. Although the pasta layers occupy a relatively thin layer in terms of thickness, the density of those layers is the highest in the crust. For $L > 70$ MeV, the mass fraction levels out for the 'PNM' sequence, always above 40%, while for the 'J35' sequence it falls off rapidly to just a few percent at $L = 115$ MeV.

Even the bubble phases of pasta can occupy a substantial portion of the crust; between 10% and 25% at low $L < 70$ MeV, remaining above 10 % for the 'PNM' seqquence and dropping to zero at $L \approx 85$ MeV for 'J35'. This is of relevance, as in the bubble phases the protons are no longer localized in space, opening up a range of possible effects such as the direct Urca process [9] and bulk superflow of protons.

In the top right panel, the MSL baseline is compared to the BD EoS and the selected Skyrmes. The mass fractions of the total pasta and bubble phases are elevated relative to the MSL results; the total pasta fraction remaining above 60% for the BD J35 sequence, and above 40% for the 'PNM' sequence, while the BD 'J35' sequence gives rise to a crust in which more than 20% of the mass is contained within the bubble phases. It is important to note that this is consistent with the fact that the transition pressures are much lower for the BD EoSs; the transition pressures set the absolute mass of the crust, which is lower for the BD models; however, the fraction of that mass in pasta and bubbles is higher. The Skyrmes have mass fractions in between the MSL and BD EoSs.

It was noted that the transition pressures are most affected by variations in the behavior of the surface energy at low proton fraction, as explored through the variation of the parameter

$p$. In the bottom left and right panels, the baseline results are compared with the results using $p = 2$ (stiffer surface energy at low proton fraction) and $p = 4$ (softer). For the p=4, the mass fractions of pasta and the bubble components are elevated slightly compared to the baseline. For p=2 the mass fractions are greatly reduced; remaining between 10% and 30% for the total pasta fraction on the 'PNM' sequence, and falling from 60% at $L$ =25 MeV down to 0% at $L$ =80 MeV on the 'J35' sequence. The bubble phases almost completely disappear for $p = 2$, existing only for $L < 50$ MeV for any sequence; the bubble fractions are raised for $p = 4$, accounting for 10%-35% of the crustal mass.

We now give some simple examples of how some bulk crust quantities of interest in physical models of neutron star phenomena are affected by the previous exploration of the CLDM. We will focus on the charge and mass number of nuclei, the shear modulus of the crust and its melting temperature, displayed in Fig. 23. All these quantities are defined only within the region of the crust in which separate nuclei exist and become undefined or the expression we use is invalid in the pasta phases.

The top left and right panels show $Z$ and $A$ over the inner crust. The baseline results are the shaded band; for a given EoS $Z$ tends to remain roughly constant, and varies by a factor of 2 from 20 to 40. Increasing the surface tension at high and low proton fractions tends to increase the nuclear size to reduce the surface energy compared to the bulk; thus $Z$ increases. The hatched band takes into account those variations through $c$ and $p$ and increases $Z$ up to about 50 in the higher density regions of the crust. The DH EoS lies along the upper bound of the baseline results; BBP diverges to much higher $Z$ at higher densities, again an artifact of the much higher surface tension. $A$ shows a similar trend; the baseline results predict $A$ to rise from between 60 and 150 at the lowest densities; higher $L$ predicts a slower rise. Increasing the surface energy increases $A$ and the rate at which it increases up, reaching towards 1000 at the transition to pasta. Again, DH runs along the upper bound of the baseline results, while BBP predicts much higher $A$ at high densities, in line with our results for high surface energy.

The shear modulus of a Coulomb lattice of positively charged nuclei in a uniform negatively charged background in the neutron star crust at a baryon number density $n_{\rm b}$ was determined through Monte-Carlo simulation [21–23] and can be written as

$$\mu = 0.1106 \left(\frac{4\pi}{3}\right)^{1/3} A^{-4/3} n_{\rm b}^{4/3} (1 - X_{\rm n})^{4/3} (Ze)^2, \tag{24}$$

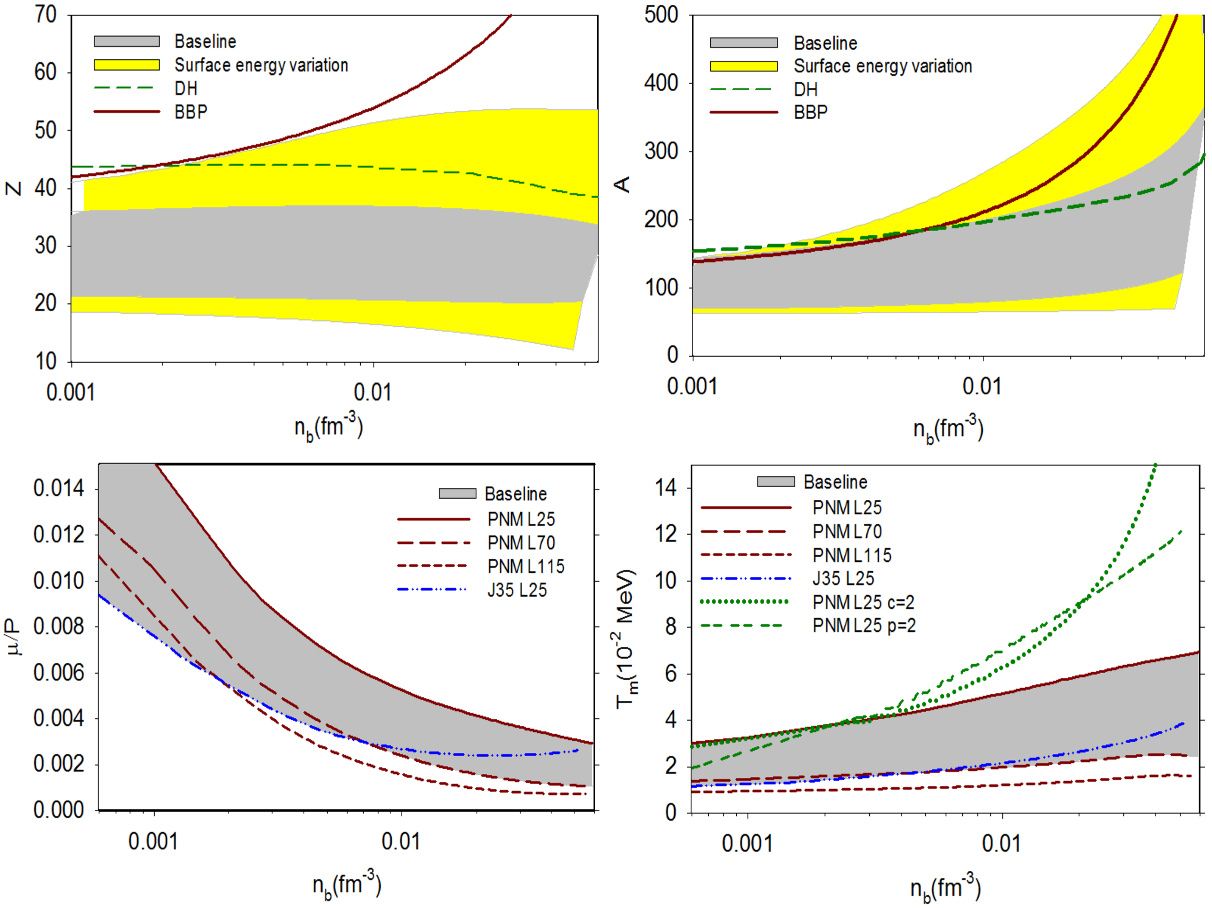

FIG. 23: (Color online) Top left and top right: charge $Z$ and mass $A$ number of nuclei in the crust up to the transition to pasta versus density for the baseline MSL EoSs (shaded area) and the variation with surface energy (hatched area) together with the results from the Douchin and Haensel EoS [41] (DH) and BBP EoS [29] (BBP). Bottom left and right: shear modulus of crust scaled by pressure and melting temperature versus density for the baseline MSL EoSs.

where the nuclei are characterized by the nucleon and proton number $A, Z$ and $X_{\rm n}$ is the fraction of neutrons not confined to the nuclei. This is the zero-temperature expression, a good approximation for neutron star temperatures below $\sim 10^8$K. Technically this is valid only when the ions (nuclei) can be treated as point charges in a uniform background of electrons; finite size effects and the dripped neutrons are not taken into account. Nevertheless, it is widely used to approximate the shear modulus of the inner crust.

The melting temperature (at which the crystalline lattice changes to a gas of ions) can be expressed as [82]

$$T_{\mathrm{m}} = \frac{(Ze)^2}{175 k_{\mathrm{B}} r_{\mathrm{C}}} \tag{25}$$

neglecting quantum effects like zero-point vibrations.

The bottom two panels of Fig. 23 show the shear modulus scaled to pressure (left) and the melting temperature (right) in terms of 0.01 MeV ($1.16 \times 10^8$ K). The baseline results for the shear modulus show a variation of a factor of about 2 throughout the inner crust; the melting temperature varies by a factor of 3 throughout the crust. The shear modulus is not as sensitive to the surface energy.

## X. CONCLUSIONS

We have constructed a set of baseline inner crust EoSs using the CLDM, spanning the experimentally constrained range of the slope of the symmetry energy $25 < L < 115$ MeV at constant $J$ over the range 25 - 35 MeV, as well as a sequence in which $J$ is allowed to vary in order for the low density EoSs to match current state-of-the-art low density PNM calculations. Consistency of the PNM constraint with the range $J$ = 25-35 MeV constrains $L$ <70 MeV; the sequences of EoSs consistent with these conditions give the following ranges for crustal parameters:

- $n_{\mathrm{cc}}$ = 0.08-0.12 fm$^{-3}$; $n_{\mathrm{p}}$ = 0.05-0.06 fm$^{-3}$. Pasta phases exist to some extent throughout the whole range $25 < L < 115$ MeV. By scaling $n_{\mathrm{cc}}$ to the symmetry energy $J$, the correlations with $L$ fall closely along the same curve, independent of the EoS used.
- $P_{\mathrm{cc}}$ = 0.35-0.8 MeV fm$^{-3}$; $P_{\mathrm{p}}$ = 0.15-0.3 MeV fm$^{-3}$. We have extended the results of [14] to show within the CLDM that $P_{\mathrm{cc}}$ correlates tightly with $L(n = 0.1\ \mathrm{fm}^{-3})$-$0.343 K_{\mathrm{sym}}(n = 0.1\ \mathrm{fm}^{-3})$ independent of $J$ and EoS used.
- The pressure throughout the crust varies by $5 < P/n^{4/3} < 15$ MeV fm.
- The volume fraction of the charged component of the crust $v \approx$ 0.001 - 0.15 in the region $n = 0.001$ up to the transition to the pasta phases $n_{\mathrm{p}}$, then rising to the crust-core transition volume fraction of 0.8-0.96.
- $X_{\mathrm{n}}$ rises rapidly from 0 at the neutron drip point to between 0.7-0.9 in the range $n = 0.005 - n_{\mathrm{p}}$ fm$^{-3}$; it then falls to its transition value of between 0.01 and 0.2.
- $r_{\mathrm{C}}$ can be roughly be described by the relation $r_{\mathrm{C}} = -14.5 \log n - 3.5 \pm 4$ fm throughout the crust.

- $x$ can roughly be described by the relation $x = -2n + 0.24 \pm 0.03$ fm in the range $n = 0.01 - 0.1$ fm$^{-3}$; at lower densities $x$ rises to $0.3 \pm 0.05$ at neutron drip density.
- The fraction of the total crust mass containing the total pasta phases lie in the range 50 - 70%. The mass fractions of the bubble phases, in which the protons are free, is in the range 10 - 25%.
- The charge and mass numbers Z and A fall in the ranges Z = 20-35 throughout most of the crust, with the lower bound dropping to Z=10 at the transition to pasta, and A = 60-200 throughout most of the crust, with the higher bound rising to 300 at the transition to pasta.

The above ranges are greater when one relaxes the requirement of $L < 70$ MeV. Note that whilst the above ranges give a good guide to the range of crustal parameters, the dependence on the symmetry energy within those ranges is more complicated, and to probe the effect of the symmetry energy and PNM EoS on neutron star phenomena, one must use crustal EoSs consistent with the core EoSs based on the symmetry energy parameters.

Other model parameters were varied to assess their effect. The surface energy at low isospin asymmetry ($\delta \rightarrow 0$) is increased by decreasing the surface symmetry energy $\sigma_\delta$ through the correlation with the bulk symmetry energy $c$. At high asymmetry, the parameter $p$ controls the strength of the surface tension, with lower $p$ resulting in a higher surface tension. Recent calculations of neutron drops suggest that $p$ might be lower than is obtained from fits to calculations involving Skyrme functionals. We show that decreasing $p$ from 3 (the baseline) to 2 significantly reduces the baseline $n_{\rm cc}$ range to 0.06 - 0.11 fm$^{-3}$ and $P_{\rm cc}$ to 0.2 - 0.75 MeV fm$^{-3}$. The mass fraction of pasta in the crust is reduced to 0.1 - 0.6 for $L < 70$ MeV, vanishing completely for $L > 70$ in the models with constant $J$. The effect of the surface symmetry-bulk symmetry parameter $c$ is much less pronounced; decreasing $c$ from the baseline value to the minimum value used, 2, reduces $n_{\rm cc}$ by $\approx 0.005$ fm$^{-3}$ and $P_{\rm cc}$ by $\approx 0.05$ MeV fm$^{-3}$. Increasing (decreasing) the surface tension can alter $Z$ by up to +10 (-5) throughout the crust.

The composition is relatively unaffected by changes to $c$ and $p$ except for the WS cell size $r_{\rm C}$ which increases by $\approx 5$ fm by decreasing either $c$ or $p$ to their minimum values. The saturation density $n_0$ has little effect on any of the crustal properties when the densities are scaled to $n_0$, except for $r_{\rm C}$ which increases by $\approx 5$ fm by lowering $n_0$ to 0.14 fm$^{-3}$. Changing

$K_0$ in the range 220-260 MeV has a small effect on the transition properties, raising or lowering $n_{\rm cc}$ by $\pm 0.003$ fm$^{-3}$, with negligible effect on the crustal composition.

Our results are consistent with other widely used crustal EoSs such as DH. Comparing their EoS with the results we obtain using the SLy4 Skyrme (as used in DH), with the baseline surface parameters, shows that DH obtain a larger $r_{\rm C}$ (still within our overall baseline region) and $Z$, suggesting that DH used lower values for the surface symmetry energy.

Thus, in order to constrain the crust composition and transition properties further, we believe the most urgent work must be done in constraining the PNM EoS, through microscopic calculations such as those discussed in section III (GCR, HS, SP) and the surface tension of nuclear clusters at low proton fraction.

We have shown that properties of the crust important in calculating the hydrodynamics and thermodynamics of neutron stars (e.g. shear modulus), as well as the thickness, mass and moment of inertia fractions of the crust, are sensitive to the EoS of uniform, neutron rich matter, especially the symmetry energy (its absolute value at saturation and the shape of the symmetry energy function with density), and, relatedly, the PNM EoS, and also to the surface tension at low proton fractions. Coupled with the sensitivity of global neutron star properties to the same EoS properties, models of phenomena with potentially observable signatures such as oscillations, heating and cooling, crustal deformations and the dynamical couplings between crust and core can be quite sensitive to the symmetry energy and PNM EoS, sensitivities that only appear significant when crust and core descriptions are consistent [2]. To that end, the sequences of crust EoSs discussed in this paper are available for use [83] in the form of both the basic EoS (pressure versus energy density and baryon number density) and an extensive set of crustal composition; appropriate crust EoSs can easily be matched to any core EoS based on their respective values of $J$ and $L$.

Finally, we have established how the basic crustal composition varies within experimental and theoretical uncertainties in the CLDM. The model, as mentioned, has some serious draw backs. The WS approximation breaks down in the highest density regions of the crust - the pasta layers - and shell effects are not taken into account. In upcoming work we shall compare the CLDM results for transition properties and composition with fully microscopic calculations of the crustal matter at the highest densities using a 3D Hartree-Fock method [84], in order to establish how much the predictions of the CLDM differ from a more realistic model.

## ACKNOWLEDGEMENTS

This work is supported in part by the National Aeronautics and Space Administration under grant NNX11AC41G issued through the Science Mission Directorate and the National Science Foundation under grants PHY-0757839 and PHY-1068022 and the Texas Coordinating Board of Higher Education under grant No. 003565-0004-2007.

## XI. APPENDIX: UNIFORM NUCLEAR MATTER EQUATIONS OF STATE

### A. MSL

The phenomenological modified Skyrme-like (MSL) model [43] will be the form for the uniform, isospin-asymmetric nuclear matter EoS we use for our baseline results. The energy as a function of density $n$ and isospin asymmetry $\delta$ is written down in a form that closely resembles the uniform nuclear matter Skyrme EoS under the Hartree-Fock approach; the advantage of the MSL function is that its free parameters can be more easily related to the properties of nuclear matter at saturation, and allow for a smooth variation of those parameters. The MSL EoS is

$$\begin{aligned} E^{\mathrm{MSL}}(n,\delta) &= \frac{\eta}{n}\left(\frac{\hbar^2}{2m_n^*}n_n^{5/3} + \frac{\hbar^2}{2m_n^*}n_p^{5/3}\right) \\ &\quad + \frac{\alpha}{2}\frac{n}{n_0} + \frac{\beta}{\sigma+1}\frac{n^\sigma}{n_0^\sigma} + E_{sym}^{loc}(n)\delta^2, \end{aligned} \tag{26}$$

$$E_{sym}^{loc}(n) = (1-y)E_{sym}^{loc}(n_0)\frac{n}{n_0} + yE_{sym}^{loc}(n_0)\left(\frac{n}{n_0}\right)^{\gamma_{\mathrm{sym}}}, \tag{27}$$

where

$$\frac{\hbar^2}{2m_n^*} = \frac{\hbar^2}{2m} + n(C_{\mathrm{eff}} + D_{\mathrm{eff}}\delta) \tag{28}$$

$$\frac{\hbar^2}{2m_p^*} = \frac{\hbar^2}{2m} + n(C_{\mathrm{eff}} - D_{\mathrm{eff}}\delta) \tag{29}$$

$\eta = (3/5)(3\pi^2)^{2/3}$, $n_0$ is the saturation density and $\alpha$, $\beta$, $\sigma$, $C_{\mathrm{eff}}$, $D_{\mathrm{eff}}$, $\gamma_{\mathrm{sym}}$, $E_{\mathrm{sym}}^{\mathrm{loc}}$ and $y$ are free parameters. $C_{\mathrm{eff}}$ and $D_{\mathrm{eff}}$ are fixed by setting the effective masses at saturation to be $m_{\mathrm{p},0}^* = 0.8m$ and $m_{\mathrm{n},0}^* = 0.7m$, where $m$ is the average nucleon mass in free space. We set

$\gamma_{\rm sym} = 4/3$; $\alpha$, $\beta$, $\sigma$ are set by $K_0$, $n_0$ and $E_0$ while $E^{\rm loc}_{\rm sym}$ and $y$ control the absolute value of the symmetry energy and its slope respectively.

### B. BD

We use as a comparison with MSL a form for the uniform, isospin-asymmetric nuclear matter EoS originally obtained by Bludman and Dover [44] and modified by Oyamatsu and Iida [45]:

$$\begin{aligned} E^{\rm BD}(n,\delta) &= \frac{\eta}{n}\left(\frac{\hbar^2}{2m_n}n_n^{5/3} + \frac{\hbar^2}{2m_n}n_p^{5/3}\right) \\ &+(1-\delta^2)\frac{v_{\rm s}(n)}{n} + \delta^2\frac{v_{\rm n}(n)}{n} \end{aligned}, \tag{30}$$

$$v_{\rm s} = a_1 n^2 + \frac{a_2 n^3}{1+a_3 n}, \tag{31}$$

$$v_{\rm n} = b_1 n^2 + \frac{b_2 n^3}{1+b_3 n}. \tag{32}$$

$v_{\rm s}$ and $v_{\rm n}$ are the potential energy densities for SNM and PNM respectively. The free parameters $a_1, a_2, a_3, b_1, b_2$ are adjusted to obtain the desired values of the saturation properties $K_0$, $n_0$, $E_0$, $J$ and $L$, while $b_3$ which controls the behavior of PNM at high densities is fixed at 1.58632 fm$^3$ as suggested in OI [10]; this parameter is analogous to $\gamma_{\rm sym}$ in the MSL model.

[1] B. Link, R.I. Epstein and J.M. Lattimer, Phys. Rev. Lett. **83**, 17, 3362 (1999).

[2] M. Gearheart, W.G. Newton, J. Hooker and Bao-An Li, accepted for publication in MNRAS (2011), arXiv:1106.4875

[3] H. Sotani, MNRAS **417**, 1, L70 (2011).

[4] L. Lindblom, B.J. Owen and G. Ushomirsky, Phys. Rev. **D62**, 084030 (2000).

[5] Y. Wu, C.D. Matzner and P. Arras, ApJ **549**, 1011 (2001).

[6] K. Glampedakis and N. Andersson, Phys. Rev. **D74**, 044040 (2006).

[7] J.M. Lattimer and M. Prakash, ApJ **550**, 1, 426 (2001).

[8] M. Urbanec, J.C. Miller and J. Rikovska-Stone, In Proceedings of RAGtime 6/7: Workshops on black holes and neutron stars, Opava, 16-18/18-20 September, 2004/2005; S. Hledk and Z.

Stuchlk, editors, Silesian University in Opava, Czech Republic, 12/2005, ISBN 80-7248-334-X, pp. 357-362 (2005)

[9] M.E. Gusakov, A.D. Kaminker, O.Y. Gnedin and P. Haensel, Astron. Astrophys. **421**, 1143-1148 (2004).

[10] K. Oyamatsu and K. Iida, Phys. Rev. **C75**, 015801 (2007).

[11] A.W. Steiner, Phys. Rev. **C77**, 035805 (2008).

[12] C. J. Horowitz and J. Piekarewicz, Phys. Rev. Lett. **86**, 5647 (2001).

[13] J. Xu, L.W. Chen, Bao-An Li and H.R. Ma, Phys. Rev. **C79**, 035802 (2009); ApJ **697**, 1549 (2009).

[14] C. Ducoin, J. Margueron, C. Providencia and I. Vidana, Phys. Rev. **C83**, 4, 045810 (2011).

[15] G. Ushomirsky, C. Cutler, L. Bildsten, MNRAS **319**, 902 (2000).

[16] B. Haskell, D.I. Jones, N. Andersson, MNRAS **373**, 1423 (2006).

[17] A. Piro, ApJ **634**, L153 (2005).

[18] A.W. Steiner and A.L. Watts, Phys. Rev. Lett. **103**, 181101 (2009).

[19] L. Samuelsson and N. Andersson, MNRAS **374**, 256 (2007).

[20] N. Andersson, K. Glampedakis and L. Samuelsson, MNRAS **396**, 894 (2009).

[21] S. Ogata and S. Ichimaru, Phys. Rev. **A42**, 8, 4867 (1990).

[22] T. Strohmayer, H.M. van Horn, S. Ogata, H. Iyetomi and S. Ichimaru, ApJ **375**, 679 (1991).

[23] A.I. Chugunov and C.J. Horowitz, MNRAS **407**, 1, L54 (2010).

[24] D.G. Ravenhall, C.J. Pethick and J.R. Wilson, Phys. Rev. Lett. **50**, 26, 2066 (1983).

[25] K. Oyamatsu, M. Hashimoto and M. Yamada, Prog. Th. Phys. **72**, 2, 373 (1984).

[26] G. Watanabe, K. Iida and K. Sato, Nucl. Phys. **A676**, 455 (2000).

[27] G. Watanabe, K. Iida and K. Sato, Nucl. Phys. **A687**, 512 (2000).

[28] G. Watanabe, K. Iida and K. Sato, Nucl. Phys. **A726**, 357 (2003).

[29] G. Baym, H.A. Bethe and C.J. Pethick, Nucl. Phys. **A175**, 225 (1971).

[30] D.G. Ravenhall, C.D. Bennett and C.J. Pethick, Phys. Rev. Lett. **28**, 978 (1972).

[31] F.D. Mackie and G. Baym, Nucl. Phys. **A285**, 332 (1977).

[32] J.M. Lattimer, F. Mackie, D.G. Ravenhall and D.N.Schramm, ApJ **213**, 225 (1977).

[33] J.M. Lattimer and D.G. Ravenhall, ApJ **223**, 314 (1978).

[34] D.Q. Lamb, J.M. Lattimer, C.J. Pethick and D.G. Ravenhall, Phys. Rev. Lett. **41**, 23, 1623 (1978).

[35] D.Q. Lamb, J.M. Lattimer, C.J. Pethick and D.G. Ravenhall, Nucl. Phys. **A360**, 459 (1981).

[36] D.Q. Lamb, J.M. Lattimer, C.J. Pethick and D.G. Ravenhall, Nucl. Phys. **A411**, 449 (1983).

[37] C.J. Pethick, D.G. Ravenhall and J.M. Lattimer, Phys. Lett. **128B**, 3,4, 137 (1983).

[38] F. Douchin, P. Haensel and J. Meyer, Nucl. Phys. **A665**, 419 (2000).

[39] K. Iida and K. Sato, ApJ **477**, 294 (1997).

[40] J.M. Lattimer, F.D.Swesty, Nucl. Phys. **A535**, 331 (1991).

[41] F. Douchin and P. Haensel, A&A **380**, 151 (2001).

[42] N. Chamel, S. Naimi, E. Khan and J. Margueron, Phys. Rev. **C75**, 5, 055806 (2007).

[43] Lie-Wen Chen, Bao-Jun Cai, Che Mong Ko, Bao-An Li, Chun Shen and Jun Xu, Phys. Rev. **C80**, 014322 (2009); Lie-Wen Chen, Che-Ming Ko, Bao-An Li and Jun Xu, Phys. Rev. **C82**, 024321 (2010).

[44] S.A. Bludman and C.B. Dover, Phys. Rev. **D22**, 6, 1333 (1981).

[45] K Oyamatsu and K. Iida, Prog.Theor.Phys. **109**, 631 (2003).

[46] J.R. Stone, J.C. Miller, R. Koncewicz, P.D. Stevenson and M.R. Strayer, Phys. Rev. **C68**, 3, 034324 (2003).

[47] W.D. Myers and W.J. Swiatecki, Nucl. Phys. **A81**, 1 (1966).

[48] P. Möller, J.R. Nix and W.D. Myers and W.J. Swiatecki, Atomic Data and Nuclear Data Tables **59**, 185 (1995).

[49] K. Pomorski and J. Dudek, Phys. Rev. **C67**, 044316 (2003).

[50] M. Liu, N. Wang, Z.-X. Li and F.-S. Zhang, Phys. Rev. **C82**, 064306 (2010).

[51] P. Danielewicz and J. Lee, Nucl. Phys. **A818**, 1-2, 36, 818 (2009).

[52] Bao-An Li, Lei-Wen Chen and Che Ming Ko, Phys. Rep. **464**, 113 (2008).

[53] M.B. Tsang, Yingzun Zhang, P. Danielewicz, M. Famiano, Zhuxia Li, W.G. Lynch and A.W. Steiner, Phys. Rev. Lett. **102**, 122701 (2009).

[54] Lie-Wen Chen, Che Ming Ko and Bao-An Li, Phys. Rev. Lett. **94**, 032701 (2005).

[55] Bao-An Li and Lie-Wen Chen, Phys. Rev. **C72**, 064611 (2005).

[56] D.V. Shetty, S.J. Yennello, G.A. Souliotis, Phys. Rev. **C76**, 024606 (2007).

[57] A. Klimkiewicz *et al*, Phys. Rev. **C76**, 051603(R) (2007).

[58] P. Danielewicz and J. Lee, AIPC Conf. Proc. **947**, 301 (2007).

[59] M. Centelles, X. Roca-Maza, X. Vinas and M. Warda, PRL **102**, 122502 (2009).

[60] Lie-Wen Chen, Che Ming Ko, Bao-An Li and Jun Xu, Phys. Rev. **C82**, 2, 024321 (2010).

[61] Chang Xu, Bao-An Li and Lie-Wen Chen, Phys. Rev. **C82**, 054607 (2010).

[62] `http://www.smith.edu/nusym11/`

[63] X. Roca-Maza, M. Centelles, X. Vinas and M. Warda, Phys. Rev. Lett. **106**, 252501 (2011).

[64] A. Akmal, V.R. Pandharipande and D.G. Ravenhall, Phys. Rev. **C58**, 1804 (1998).

[65] J. Carlson, J. Morales, V.R. Pandharipande and D.G. Ravenhall, Phys. Rev. **C68**, 025802 (2003).

[66] A. Schwenk and C.J. Pethick, Phys. Rev. Lett. **95**, 160401 (2005).

[67] A. Gezerlis and J. Carlson, Phys. Rev. **C77**, 032801 (2008).

[68] K. Hebeler and A. Schwenk, Phys. Rev. **C82**, 014314 (2010).

[69] S. Gandolfi, J. Carlson and S. Reddy, arXiv:1101.1921.

[70] Chang Xu, Bao-An Li and Lie-Wen Chen, Phys. Rev. **C82** 054607 (2010).

[71] D.G. Ravenhall, C.J. Pethick and J.M. Lattimer, Nucl. Phys. **A407**, 571 (1983).

[72] J.M. Lattimer, C.J. Pethick, D.G. Ravenhall and D.Q. Lamb, Nucl. Phys. **A432**, 646 (1985).

[73] C.P. Lorenz, PhD Thesis, University of Illinois.

[74] C.P. Lorenz, D.G. Ravenhall and C.J. Pethick, Phys. Rev. Lett. **70**, 4, 379 (1993).

[75] W.D. Myers and W.J. Swiatecki, Ann. Phys. **55**, 395 (1969).

[76] P. Danielewicz, Nucl. Phys. **A727**, 3-4, 233 (2003).

[77] A.W. Steiner, M. Prakash, J.M. Lattimer and P.J. Ellis, Physics Reports **411**, 6, 325 (2005).

[78] P.-G. Reinhard, M. Bender, W. Nazarewicz and T. Vertse, Phys. Rev. **C73**, 014309 (2006).

[79] S. Gandolfi, J. Carlson and Steven C. Pieper, Phys. Rev. Lett., **106**, 1, 012501 (2011).

[80] C.J. Pethick and D.G. Ravenhall, Annu. Rev. Nucl. Part. Sci. **45**, 429 (1995).

[81] K. Nakazato, K. Oyamatsu and S. Yamada, Phys. Rev. Lett. **103**, 132501 (2009).

[82] P. Haensel, A.Y. Potekhin and D.G. Yakovlev, Neutron Stars 1: Equation of State and Structure, Astrophysics and Space Science Library, vol. 326, (Springer, New York, U.S.A., 2007).

[83] `http://williamnewton.wordpress.com/ns-eos`

[84] W.G. Newton and J.R. Stone, Phys. Rev. **C79**, 055801 (2009).